Cronfa - Swansea University Open Access Repository

_____

This is an author produced version of a paper published in :
Global Change Biology

_____

_____

Paper:

Helbig, M., Wischnewski, K., Kljun, N., Chasmer, L., Quinton, W., Detto, M. & Sonnentag, O. (2016). Regional atmospheric cooling and wetting effect of permafrost thaw-induced boreal forest loss. *Global Change Biology*
http://dx.doi.org/10.1111/gcb.13348

_____

Regional atmospheric cooling and wetting effect of permafrost thaw-induced boreal forest loss

Helbig M[1]*, Wischnewski K[1], Kljun N[2], Chasmer L[3], Quinton W L[4], Detto M[5], Sonnentag O[1]

[1]Université de Montréal
Département de géographie & Centre d'études nordiques
520 Chemin de la Côte Sainte-Catherine
Montréal, QC H2V 2B8, Canada

[2]Swansea University
Department of Geography
Swansea, UK

[3]University of Lethbridge
Department of Geography
Lethbridge, AB, Canada

[4]Wilfrid Laurier University
Cold Regions Research Centre
Waterloo, ON, Canada

[5]Smithsonian Tropical Research Institute
Panamá, República de Panamá

*corresponding author:
tel. 438-826-1985
email: manuel.helbig@umontreal.ca

Abstract

In the sporadic permafrost zone of North America, thaw-induced boreal forest loss is leading to the expansion of permafrost-free wetlands. These land cover changes alter landscape-scale surface properties with potentially large, however, still unknown impacts on regional climates in the boreal zone. In this study, we use a combination of nested eddy covariance flux towers and satellite remote sensing to characterise the impacts of boreal forest loss on albedo, eco-physiological and aerodynamic surface properties, and turbulent energy fluxes of a lowland boreal forest region in the Northwest Territories, Canada. Planetary boundary layer modelling is used to estimate the potential impact of these changes on regional air temperature and atmospheric moisture. Our results show that thaw-induced conversion of forests to wetlands increases albedo, bulk surface conductance for water vapour, and aerodynamic surface temperature. At the same time, heat transfer efficiency is reduced. These shifts in land surface properties increase latent at the expense of sensible heat fluxes, thus, drastically reducing Bowen ratios. Due to the lower albedo of forests and their masking effect of highly reflective snow, available energy is lower in wetlands, especially in late winter. Modelling results show that a conversion of a present-day boreal forest-wetland to a hypothetical homogeneous wetland landscape could induce a maximum near-surface cooling effect on regional air temperatures of 3 to 4 °C in late winter and 1 to 2 °C in summer. An atmospheric wetting effect in summer is indicated by a maximum increase in water vapour mixing ratios of 2 mmol mol^{-1} with maximum boundary layer heights being reduced by about a third of the original height. In fall, simulated air temperature and atmospheric moisture do not differ significantly between the two scenarios. Permafrost thaw-induced forest loss may, therefore, modify regional precipitation patterns and partly compensate warming trends in the boreal zone.

Introduction

A large proportion of North America's high-latitude landscapes contain permafrost, perennially cryotic ground, spanning from the tundra in the north, over subarctic woodlands, to the boreal forests further south (Strong *et al.*, 1989). About 60 % of North America's boreal forests lie in the zones of discontinuous permafrost (50 % to <90 % of the land surface contains permafrost) and sporadic permafrost (10 % to <50 %) (e.g. Olson *et al.*, 2001; van Everdingen, 2005; Gruber, 2012; Helbig *et al.*, 2016). Across the boreal zone, rapid rates of climate warming are already occurring and are projected to intensify in the near future (Hartmann *et al.*, 2013).

Climate change is expected to alter the composition and structure of boreal forest and wetland ecosystems inducing strong biophysical and biogeochemical feedbacks to regional and global climates through altered land-atmosphere interactions (e.g. Chapin *et al.*, 2000; Meissner *et al.*, 2003; Chapin *et al.*, 2005; Bonan, 2008; Alkama & Cescatti, 2016). At high latitudes, biophysical feedbacks to regional climates mainly imply changes in the surface fluxes of sensible and latent heat (Bonan, 2008). Vegetation composition and structure strongly determine physical and biological land surface properties such as albedo, surface temperature, and bulk aerodynamic and surface conductance (Eugster *et al.*, 2000; Kasurinen *et al.*, 2014). Thus, vegetation changes alter surface properties and consequently also turbulent energy flux regimes (e.g. Snyder *et al.*, 2004; Davin & de Noblet-Ducoudré, 2010; Baldocchi & Ma, 2013; Luyssaert *et al.*, 2014; Alkama & Cescatti, 2016). For example, a shift from deciduous to coniferous forests decreases surface conductance and increases the Bowen ratio, the ratio of sensible to latent heat flux (Eugster *et al.*, 2000). The modified diurnal heat input to the regional planetary boundary layer (PBL) leads to altered diurnal PBL growth dynamics affecting its effective heat capacity, entrainment of dry air from the free atmosphere, and consequently, feedbacks to regional air temperatures and convective rainfall (e.g. Baldocchi *et al.*, 2000; Juang *et al.*, 2007a; Esau *et al.*, 2012). In addition, boreal forests exert a strong biophysical influence on regional air temperatures even at latitudes far outside their zone of distribution due to its effect on the general circulation of the atmosphere (Bonan *et al.*, 1992; Snyder *et al.*, 2004).

At the southern limit of the permafrost zone in Canada and Alaska, warming air temperatures cause widespread thaw. In recent decades, this thaw has resulted in disappearance of forested permafrost plateaus and conversion of boreal forests to wetlands (e.g. Camill & Clark, 1998; Camill, 1999a; Jorgenson *et al.*, 2001; Quinton *et al.*, 2011; Helbig *et al.*, 2016; Lara *et al.*, 2016). Permafrost plateaus dominated by coniferous tree species rooted in raised, thick organic soils; and treeless, seasonally frozen wetlands are the two predominant land cover types of the lowland boreal landscapes in the discontinuous and sporadic permafrost zones of northwestern Canada (Zoltai & Tarnocai, 1975; Tarnocai, 2006). The proportional coverage of forests and wetlands is affected by the degree of permafrost thaw (Quinton *et al.*, 2011). Forested permafrost plateaus and wetlands differ in their soil moisture and temperature regimes with wetlands being substantially wetter and warmer (Chasmer *et al.*, 2011a; Quinton & Baltzer, 2013; Baltzer *et al.*, 2014; Fig. S1). Root inundation and mortality

inhibits tree growth in wetlands, resulting in sharp transitions of vegetation composition and structure from forest to wetland (e.g. Camill, 1999b; Baltzer *et al.*, 2014).

Despite the importance of boreal forests in the permafrost zone for the global and regional climates (Chapin *et al.*, 2000), local- to regional-scale responses of land-atmosphere interactions to thaw-induced land cover change are still poorly understood. It remains unclear as to how such vegetation shifts may affect turbulent energy fluxes and how these might modify regional trends in air temperature and atmospheric moisture. Compared with deforestation in the temperate and tropical zones and to wildfires in the boreal zone (e.g. Liu *et al.*, 2005; Randerson *et al.*, 2006), the biophysical consequences of permafrost thaw-induced boreal forest loss and ultimately disappearance have received little attention. A better understanding of the impacts of disappearing permafrost on regional turbulent energy flux regimes is important to project the trends of air temperature and atmospheric moisture in the boreal zone (Chapin *et al.*, 2000) and to evaluate the performance of current land surface schemes and terrestrial biosphere models (Fisher *et al.*, 2014). In this study, we aim to:
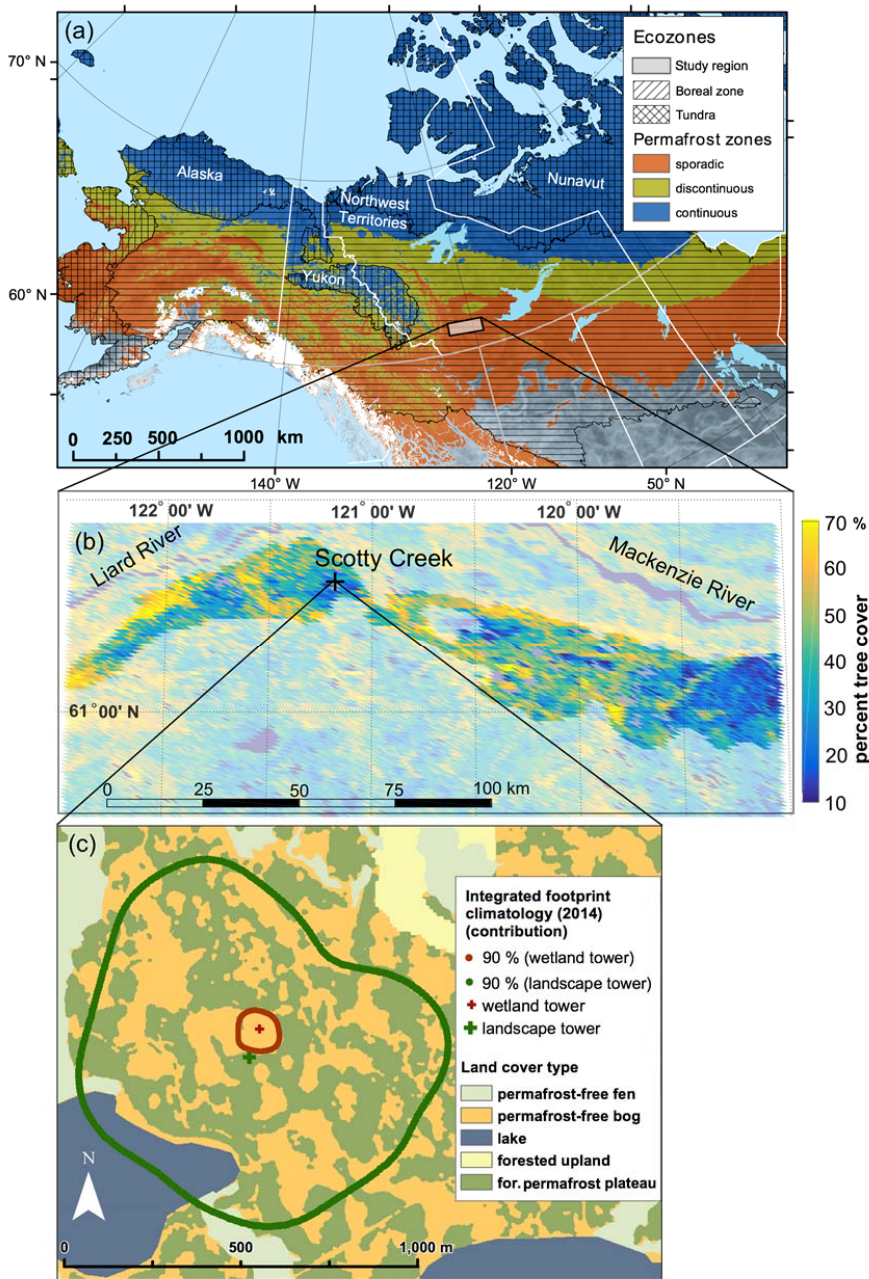
(1) quantify the impact of permafrost disappearance and concurrent tree cover loss in the zone of sporadic permafrost on turbulent energy flux dynamics,

(2) identify the landscape scale ($\sim$1 km^2) changes in land surface properties causing changes in turbulent energy flux dynamics,

(3) quantify boreal tree cover controls on land surface properties on a regional scale ($\sim$4000 km^2), and

(4) estimate potential effects of thaw-induced shifts in land cover on regional air temperature and atmospheric moisture.

Materials and Methods

Study site

Scotty Creek (61°18' N; 121°18' W, NT, Canada) is a 152-km^2 watershed located in the southern Taiga Plains and is situated in the zone of sporadic permafrost (Fig. 1a). The southern part of the watershed is characterised by rapidly thawing permafrost resulting in a mosaic of forested permafrost plateaus, wetlands, forested uplands, and shallow thaw lakes (Chasmer *et al.*, 2014). Permafrost-free wetlands occur as collapse-scar bogs that receive some lateral inflow of water from the surrounding forests, and as channel fens that route water towards the watershed outlet (National Wetlands Working Group, 1997; Quinton *et al.*, 2009). Organic soils are widespread in the region with peat thickness ranging from 0.6 m to 5 m (Aylsworth *et al.*, 1993). Black spruce (*Picea mariana*) is the dominant tree species on the forested permafrost plateaus. The understorey and ground cover on the permafrost plateau mainly consists of Labrador tea (*Rhododendron groenlandicum*), ground lichen (*Cladonia* spp.), and *Sphagnum fuscum* and *capillifolium*. Collapse-scar bogs are mainly populated by *Sphagnum balticum & magellanicum* and ericaceous (Garon-Labrecque *et al.*, 2015).

Fig. 1: (a) Location of the Scotty Creek watershed, zones of sporadic (10 % - <50% areal permafrost coverage), discontinuous (50% - <90%), and continuous (≥90%) permafrost (data from Gruber, 2012), and areal extent of the boreal and tundra zones (data from Olson *et al.*, 2001). **(b)** Percent tree cover in 2010 in the southern Taiga Plains. Pixels with surface elevations <250 m a.s.l. and >300 m a.s.l. are shaded. **(c)** Land cover types in the vicinity of the two flux towers (Chasmer *et al.*, 2014) and their flux footprint climatologies for the period April to November 2014.

The mean annual air temperature (1981-2010) in Fort Simpson, ca. 60 km north of Scotty Creek, is -2.8 ºC with a mean January air temperature of -24.2 ºC and a mean July air temperature of 17.4 ºC. The long-term mean of total annual precipitation (1981-2010) is 388 mm. Snowfall accounts for about 50 % of the total annual precipitation. During the study period, from May to November 2013 and April to November 2014, mean air temperature was 2.1 ºC and 0.2 ºC warmer and total precipitation was 73 mm (26 %) and 87 mm (29 %) lower than the long-term average, respectively (Environment Canada, 2014).

Eddy covariance measurements

Turbulent fluxes of momentum and energy were measured using the eddy covariance technique at two nested micrometeorological towers at Scotty Creek (Baldocchi, 2014). One eddy covariance system was mounted on top of a 15-m tower with flux footprints originating from a boreal forest-wetland landscape (hereafter referred to as "landscape tower", measurement period: 11 May 2013 to 07 November 2014). A second system was installed on a 2-m tower at 1.9 m above the ground surface (hereafter referred to as "wetland tower", measurement period: 12 April 2014 to 07 November 2014) with flux footprints originating from a wetland just north of the landscape tower and within its flux footprint (Fig. 1c).

The eddy covariance instrumentation, identical at both towers, included a sonic anemometer (CSAT3A, Campbell Scientific Inc., Logan, UT, USA) and a CO_2/H_2O open-path infrared gas analyser (EC150, Campbell Scientific Inc.), both operating at 10 Hz frequencies. Friction velocity (u_*; m s^{-1}), sensible (H, W m^{-2}) and latent heat fluxes (LE, W m^{-2}) were computed using the EddyPro software (version 5.2, LI-COR Biosciences, Lincoln, NE, USA). For the landscape tower, a planar fit method was deployed to rotate the coordinate system of the sonic anemometer into the mean streamlines of the wind field (Wilczak *et al.*, 2001). To account for small seasonal changes in the orientation of the sonic anemometer due to potential variations of the wetland surface, a double rotation method was applied for the wetland tower, so that the half-hourly mean vertical wind velocity equalled zero. Further corrections were applied to take into account spikes in the high-frequency time series (Vickers & Mahrt, 1997), humidity effects on sonic temperature (Dijk *et al.*, 2004), block averaging of half-hour time series, time lag detection, spectral attenuations (Moncrieff *et al.*, 1997; Moncrieff *et al.*, 2004), and air density fluctuations for water vapour fluxes (Webb *et al.*, 1980).

Supporting measurements

Both, the landscape and the wetland tower were equipped with a four-component net radiometer (CNR4, Kipp & Zonen, Delft, The Netherlands) to measure incoming and outgoing short- and longwave radiation fluxes at a height of 13.4 m and 2.1 m, respectively. Following Schmid (1997), we found that the radiometric footprint (80 % contour) at the landscape tower contained 77 % forest with the remaining 23 % being wetland. The radiometric footprint at the wetland tower consisted only of

wetland. Therefore, the radiation fluxes at the landscape and the wetland tower were considered to represent forest and wetland surfaces, respectively. Air temperature and relative humidity probes (HC2-S3, Rotronic AG, Bassersdorf, Switzerland) were installed at 15 m and at 2.6 m at the landscape and the wetland tower, respectively. Soil heat flux at 8 cm below the moss surface at the forest and at the wetland was measured in a hummock and hollow using two ground heat flux plates (HFT3, Hukseflux, Delft, The Netherlands) at each site. To calculate soil heat storage between the heat flux plates and the moss surface, half-hourly changes in soil temperatures at 2 cm, 4 cm, and 8 cm below the surface (TCAV, Campbell Scientific Inc. & Type "T", Omega Engineering, USA) were used assuming a constant heat capacity of the peat above the heat flux plate of 2 MJ m^{-3} K^{-1} (Hayashi *et al.*, 2007). Snow depth was measured in the forest and in the wetland using an ultrasonic distance sensor (SR50, Campbell Scientific Inc.). Snow density was measured on ten days during late winter 2014 between 25 March and 22 April using a snow tube. Snow melt energy flux was calculated for the forest and the wetland based on measured half-hour changes in snow depth using the SR50, the mean snow density and the latent heat of fusion of water.

Footprint modelling

To resolve the spatial heterogeneity within the flux footprints of the two eddy covariance systems, we ran the 2D footprint parameterisation of Kljun *et al.* (2015) for each tower providing not only the extent but also the width of footprints. Similar to the model of Kljun *et al.* (2004), this parameterisation is based on the Lagrangian particle dispersion footprint model of Kljun *et al.* (2002) and is valid for convective to stable boundary layer conditions. The footprint model was used to calculate the per-grid cell flux contributions for a discretised study area for every half-hour. Roughness lengths for momentum (z_{0m}; m) and zero-plane displacement heights (d_0; m) for each half-hour were derived from high-frequency sonic anemometer data to account for the spatial heterogeneity in canopy height and geometry in the proximity of the towers (see A1 & Supplementary material). The relative half-hourly flux contributions of each land cover type to the total flux were calculated as the weighted sum of the respective per-grid cell flux contributions. The 90-% flux footprints of the landscape tower mainly contained a mix of wetlands and forests, while the wetland tower predominantly contained surfaces from one ecosystem, the wetland (Fig. 1c).

Post-processing of eddy covariance measurements

A three-class quality flag system according to Mauder & Foken (2011) was used to remove half-hourly periods in the time series that do not meet steady-state conditions or when turbulence was not fully developed (quality flags 1 & 2). Remaining outliers were filtered using a spike detection algorithm (Papale *et al.*, 2006). To ensure the comparability between flux measurements at the landscape and the wetland tower, the energy balance closure (EBC) for the two towers was assessed. After applying a u_*-threshold filter ($u_* = 0.2$ m s^{-1}) and removing wetland tower fluxes with less than 95 % contributions

from the wetland, the EBC was 0.79 and 0.78 for the landscape and the wetland tower, respectively (see A2). These values are in good agreement with Stoy *et al.* (2013) who reported a mean EBC of 0.76±0.13 and of 0.88±0.23 for seven wetlands and 47 evergreen needle-leaf forest sites, respectively.

Experimental errors in eddy covariance measurements are a combination of systematic and random errors (Moncrieff *et al.*, 1996). The potential systematic error derived from the EBC analysis (~20 %) does not hamper the comparability of H and LE between the two towers, assuming that the EBC residuals are similarly attributed to H and LE for the landscape and the wetland tower. Maximum systematic errors of LE measurements are estimated to be ±8 % based on an intercomparison study of the open-path EC150 with closed-path infrared gas analysers (Helbig *et al.*, submitted).

Random errors in H and LE for all flux averaging periods were estimated as the standard deviation of H and LE for similar meteorological conditions and flux footprints within a time window of ±7 days as described by Lasslop *et al.* (2008). Random errors in H and LE were used in regression analyses after York *et al.* (2004), accounting for errors in both the dependent and the independent variables. Mean random errors were 16.3 W m^{-2} and 9.1 W m^{-2} in H, and 12.2 W m^{-2} and 14.5 W m^{-2} in LE for the landscape and the wetland tower, respectively, and increased with the magnitude of H and LE (Fig. S5).

Landscape-scale surface properties

Albedo and radiometric surface temperature represent two surface properties that are sensitive to changes in ecosystem structure and composition (e.g. Betts & Ball, 1997; Juang *et al.*, 2007; Lee *et al.*, 2011), thus strongly affecting land-atmosphere interactions in the boreal zone (e.g. Betts *et al.*, 2001). Tower-based radiation measurements over the wetland (2014) and over the forest (2013 & 2014) were used to assess the effects of thaw-induced forest loss on landscape-scale albedo and radiometric surface temperature. Aerodynamic surface properties such as bulk aerodynamic conductance for heat and water vapour (g_H; m s^{-1}; see Supplementary material) and bulk surface conductance for water vapour (g_s; m s^{-1}) were derived using Monin-Obukhov similarity theory (Garratt, 1994; Betts *et al.*, 1999). We derived aerodynamic surface temperature (T_{as}; K) for the flux footprints from measured H and modelled g_H using the following bulk transfer relationship:

$$H = \rho C_p g_H (T_{as} - T_a) \qquad (2)$$

where ρ is air density [kg m^{-3}] and C_p is the heat capacity of air [J kg^{-1} K^{-1}].

Aerodynamic surface temperature is directly related to the turbulent heat exchange between land surface and overlying atmosphere. Thus, T_{as} differs from radiometric surface temperature, which represents a weighted soil and canopy temperature as function of viewing angle of the thermal-infrared radiometer mounted on tower- (Kustas *et al.*, 2006; Detto *et al.*, 2006) or satellite-platforms (Wan, 2014).

Similarly, we obtained a bulk formulation for *LE* by assuming the same bulk aerodynamic conductance as for sensible heat (g_H) and by adding a bulk surface conductance term, g_s (Betts *et al.*, 1999):

$$LE = \lambda \left(\frac{g_H g_s}{g_H + g_s}\right) [q_s(T_{as}) - q_a] \qquad (3)$$

where λ is the latent heat of vapourisation [J kg^{-1}], q_s is the saturated specific humidity of air at T_{as} [kg kg^{-1}] and q_a is the specific humidity of air at measurement height [kg kg^{-1}].

Increasing wetland coverage in the boreal forest-wetland landscape may affect the response of g_s to variations in vapour pressure deficit (*VPD*; kPa) and incoming shortwave radiation (*SW$_{in}$*; W m^{-2}). We applied a boundary line analysis by fitting non-linear *VPD* and *SW$_{in}$* models to the upper boundary of half-hourly g_s for three flux footprint classes with increasing wetland contributions (e.g. Grelle *et al.*, 1999; Igarashi *et al.*, 2015): a "low wetland class" with footprint contributions from wetlands <63 %, a "medium wetland class" with contributions from wetlands between 63 % and 95 %, and a "high wetland class" with contributions from wetlands >95 % (i.e. from the wetland tower). Only the maximum g_s in each *VPD* and *SW$_{in}$* bin (*G$_{s\_bound}$*, m s^{-1}) were selected to minimise reductions in g_s due to other environmental drivers (see A3).

Regional-scale patterns of albedo and radiometric surface temperature

To assess regional effects of permafrost thaw-induced tree cover loss on albedo and radiometric surface temperature (T_{rs}; K), we analysed several MODIS satellite products for one area-of-interest in the southern Taiga Plains (~4000 km^2, Fig. 1b). These products included percent tree cover from the annual MOD44B Vegetation Continuous Field product, white-sky albedo from the 16-day MCD43B3 Albedo product, and day- and nighttime T_{rs} from the 8-day MOD11A2 Land Surface Temperature/Emissivity product for the years 2000 to 2015. White-sky albedo does not account for the presence of a direct radiative component and is therefore not a function of solar angle and atmospheric conditions, making it suitable for the assessment of spatial variations in albedo in response to changes in surface characteristics (Schaepman-Strub *et al.*, 2006, Jin *et al.*, 2012).

Surface elevation from the MODIS Geolocation product (MOD03) was used to mask pixels with elevations below 250 m a.s.l. and above 300 m a.s.l. to minimise altitudinal effects on T_{rs} (e.g. Li *et al.*, 2015). Scotty Creek is located at 285 m a.s.l. Pixels classified as open water bodies by the MODIS Land Water Mask (MOD44W) were discarded from the analysis. Only white-sky albedo and T_{rs} pixels with good quality flags and with error flags indicating an average T_{rs} error ≤3 K were analysed. To remove thermal anomalies in T_{rs} due to wildfires, we masked all pixels identified as affected by active fires with low to high confidence by the MODIS Thermal Anomalies & Fire product (MOD14A1). All datasets were resampled to a spatial resolution of 1 km^2.
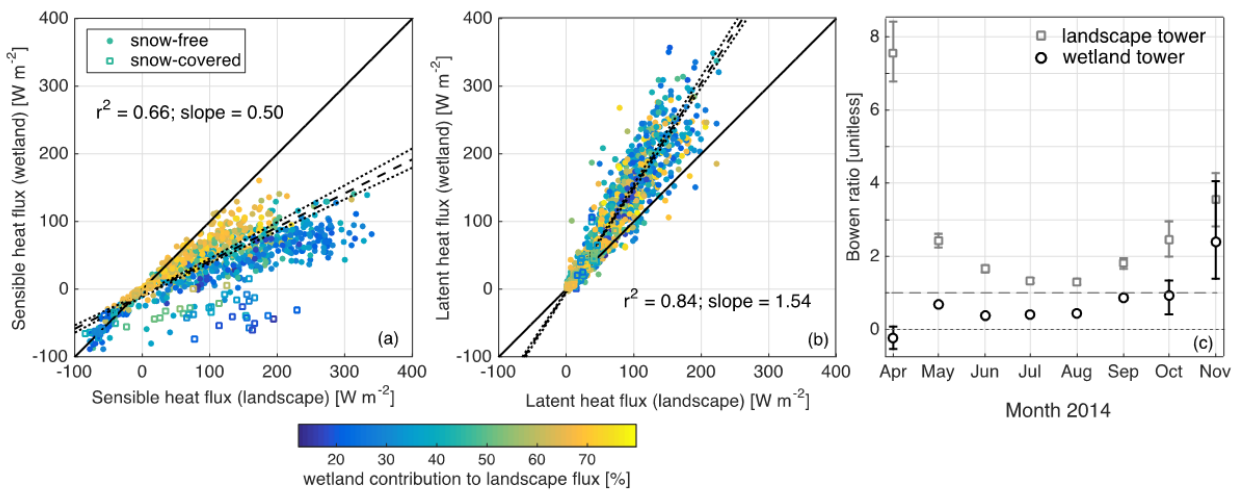
Planetary boundary layer modelling

We assessed the potential impact of a conversion of the present-day heterogeneous boreal forest-wetland to a hypothetical homogeneous permafrost-free, treeless wetland landscape on potential air temperature (θ_m; K) and water vapour mixing ratio (q_m; mol mol^{-1}) in the PBL using a clear-sky PBL model (McNaughton & Spriggs, 1986; Baldocchi & Ma, 2013; see A4). We ran the PBL model using u_*, H and LE from the landscape (representing a present-day heterogeneous landscape with permafrost) and the wetland tower (as a proxy for a hypothetical homogeneous permafrost-free landscape) as forcing and compared the diurnal θ_m and q_m dynamics of the two scenarios. The model inputs H and LE were corrected for the observed lack of EBC maintaining the Bowen ratio (Twine *et al.*, 2000). To illustrate diurnal dynamics of θ_m and q_m for the two scenarios, we analyse modelling results for one clear-sky day in the summer with no gaps in the model input time series (22 June 2014: 0800 - 2100 Mountain Standard Time (MST)). The mean footprint contributions for the landscape tower fluxes on that day were 40 % from wetlands, 56 % from forested peat plateaus, and 4 % from the lake. These contributions are representative for the present-day landscape composition in the southern part of the Scotty Creek watershed that consisted of 57 % ± 8 % and 52 % ± 9 % forested permafrost plateaus in 2000 and 2010, respectively (Baltzer *et al.*, 2014). Additionally, we ran the PBL model for a total of 49 days between 15 May 2014 and 08 October 2015 and derived daily differences in θ_m and q_m at 1800 MST between the two landscape scenarios (see A4 for selection criteria for modelled days). We compare the PBL dynamics as observed over the present-day boreal forest-wetland landscape to a hypothetical permafrost-free wetland landscape. However, it needs to be emphasised that complete disappearance of permafrost is likely to enhance large-scale drainage conditions (e.g. Connon *et al.*, 2014). The current conditions at the studied wetland site may therefore not be directly representative of a future, potentially drier, permafrost-free boreal landscape. Hence, the modelled absolute changes in θ_m and q_m should be seen as an upper limit.

Results

Changes in turbulent energy fluxes

At the end of winter in May 2014, a frost layer with a maximum depth of about 80 cm was observed in the wetland (Fig. S1). The mean water table between April and November 2014 was 15 cm below the moss surface. In contrast, a maximum thawed layer of 40 cm overlaid cryotic soil between May and September 2014 in the forest and the decrease in water table level closely followed thaw depth during the summer. In 2014, the snowmelt at the forest and the wetland occurred at the end of April and the ground was snow-covered again in October (Fig. S1). During the snow-cover period in late winter, half-hourly H at the wetland tower (H_{WET}) was negative most of the time, while H at the landscape tower (H_{LAND}) already reached maximum values of 200 W m^{-2} (Fig. 2a). At the same time, the largest mean midday (1200 – 1500 MST) Bowen ratio was observed for the landscape tower with 7.6±0.8 (± 95 % CI of mean), while the mean midday Bowen ratio at the wetland tower was the lowest with -0.3±0.3 (Fig. 2c). Between May and November 2014, H_{WET} amounted to about 50 % of H_{LAND} and the

10

ratio of the two fluxes approached unity with higher contributions of wetlands in the flux footprints of the landscape tower (Fig. 2a, a two-sample non-parametric Kolmogorov-Smirnov test indicates that the slope of H_{LAND} against H_{WET} increased significantly from 0.47 to 0.64 [p <0.001] for H_{LAND} with wetland contributions ≤36 % (75th percentile) and ≥63 % (25th percentile), respectively). In contrast, half-hourly LE at the wetland tower (LE_{WET}) was about 54 % larger than LE at the landscape tower (LE_{LAND}, Fig. 2b). Slopes of LE_{LAND} against LE_{WET} were closer to unity with increasing contributions of wetlands to LE_{LAND} (slope decreased significantly from 1.63 to 1.47 [p <0.001] for LE_{LAND} with wetland contributions ≤36 % and ≥63 %, respectively). Monthly mean midday Bowen ratios in the snow-free period ranged from 1.3 in July to 2.5 in October and from 0.4 in June to 0.9 in October at the landscape and the wetland tower, respectively (Fig. 2c). The total half-hourly turbulent energy flux ($H + LE$) was 13 % smaller at the wetland tower compared to the landscape tower (slope = 0.87, $r^2 = 0.86$).
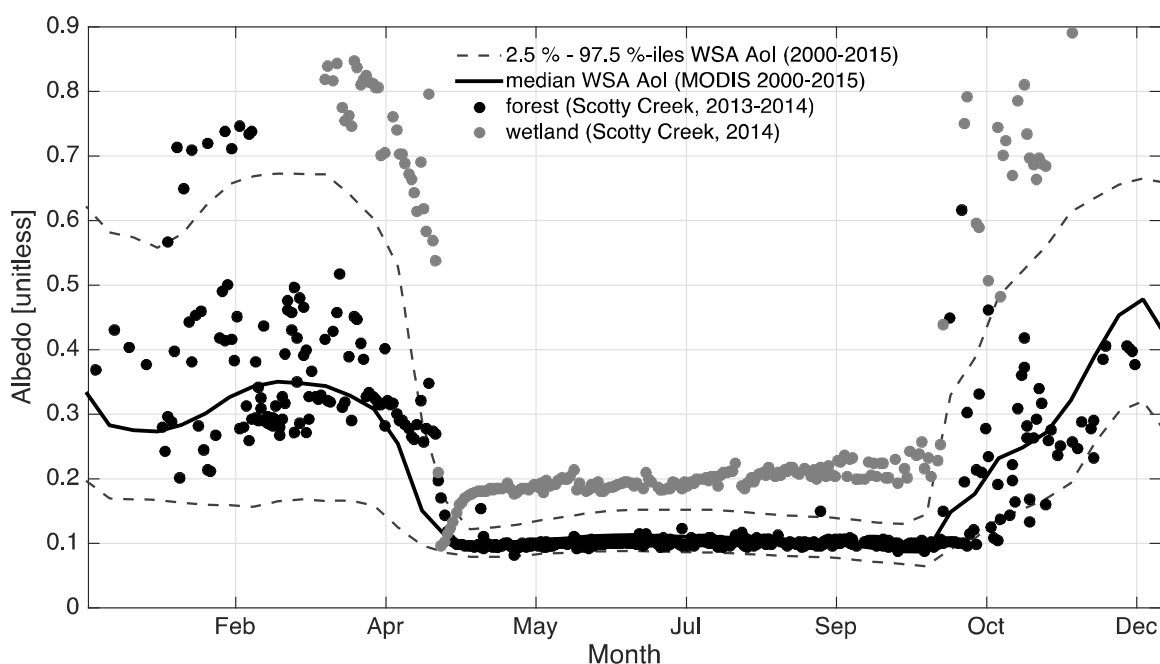

Fig. 2: **(a)** Turbulent sensible and **(b)** latent heat fluxes at the landscape (over a boreal forest-wetland landscape) and at the wetland tower (over a permafrost-free wetland) between 12 April and 07 November 2014. Colors of dots indicate relative contributions of wetlands to landscape tower fluxes. Best-fit lines with errors in both variables (York *et al.*, 2004) for the snow-free period are indicated as black dashed lines and slopes were significant at α = 0.001. Dotted black lines indicate 95 % confidence intervals (CI) of the regression as derived from 1000 bootstrap simulations of the data. **(c)** Monthly mean midday (1200 – 1500 MST) Bowen ratio (sensible heat flux/latent heat flux) for the landscape and the wetland tower. Error bars indicate the 95 % CI of the means.

Changes in surface properties

Albedo

Albedo determines how much shortwave radiation is reflected at the surface and, therefore, partly controls the available energy to generate H and LE. Between April and November 2014, the wetland albedo was consistently higher than the forest albedo, except for a three-day period (28 – 30 April

2014) shortly after snowmelt when the wetland was flooded (Fig. S2). Maximum differences in albedo of 0.5 were observed during the snow cover period (April & October – November 2014). During the snow-free period, the wetland albedo was about 0.1 higher than the forest albedo. The regional median albedo (2000 – 2015; ~4000 km^2) in the southern Taiga Plains, surrounding Scotty Creek (Fig. 1b), showed similar seasonal dynamics as the albedo measured at the two towers. Median percent tree cover of the region was 35 % (2.5 %-ile: 9 %, 97.5 %-ile: 69 %). The forest albedo at Scotty Creek corresponded to the values at the lower end of the distribution of regional albedo, whereas the wetland albedo was consistently higher than the 95 % confidence interval (except for the flooded period, Fig. 3).
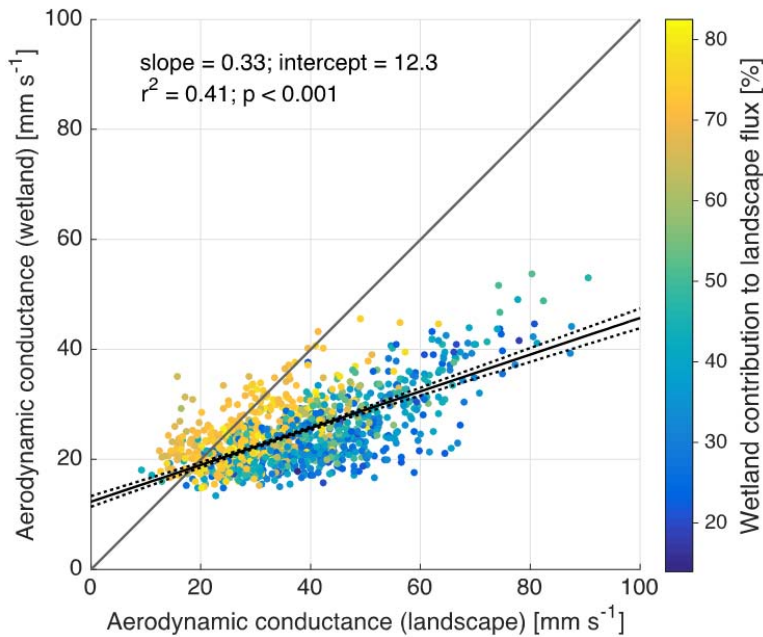

Fig. 3: Daily albedo of a boreal forest on a permafrost plateau (black dots, 2013-2014) and an adjacent permafrost-free wetland (gray dots, 2014), derived from four-component net radiometers at 1200 MST, and median (solid line, 2000-2015) and 2.5 %- and 97.5 %-iles (dotted lines) of 8-day 1-km white-sky albedo (WSA) across a ~4000 km^2 area-of-interest (AoI) in the southern Taiga Plains (derived from MCD43B3). Percentiles show spatial variability across the AoI.

Aerodynamic conductance

The median bulk aerodynamic conductance for heat (g_H), derived from turbulence data at the landscape tower, was 37.8 mm s^{-1} (2.5 %-ile: 15.8 mm s^{-1}, 97.5 %-ile: 69.8 mm s^{-1}) and 23.7 mm s^{-1} (2.5 %-ile: 16.6 mm s^{-1}, 97.5 %-ile: 40.8 mm s^{-1}) at the wetland tower. Differences between g_H at the landscape and the wetland tower decreased with increasing contributions of wetlands to the landscape fluxes (Fig.

4). Median weighted LiDAR-derived canopy height (see A1) within the flux footprints was 2.0 m (2.5 %-ile: 1.1 m, 97.5 %-ile: 3.7 m) and 0.3 m (2.5 %-ile: 0.1 m, 97.5 %-ile: 0.4 m) for the landscape and the wetland tower, respectively. Surface roughness length (z_0) increased linearly with the mean weighted LiDAR-derived canopy height ($r^2 = 0.75$, $p < 0.001$) and flux footprint contributions of wetlands ($r^2 = 0.57$, $p < 0.001$; Fig. S3).
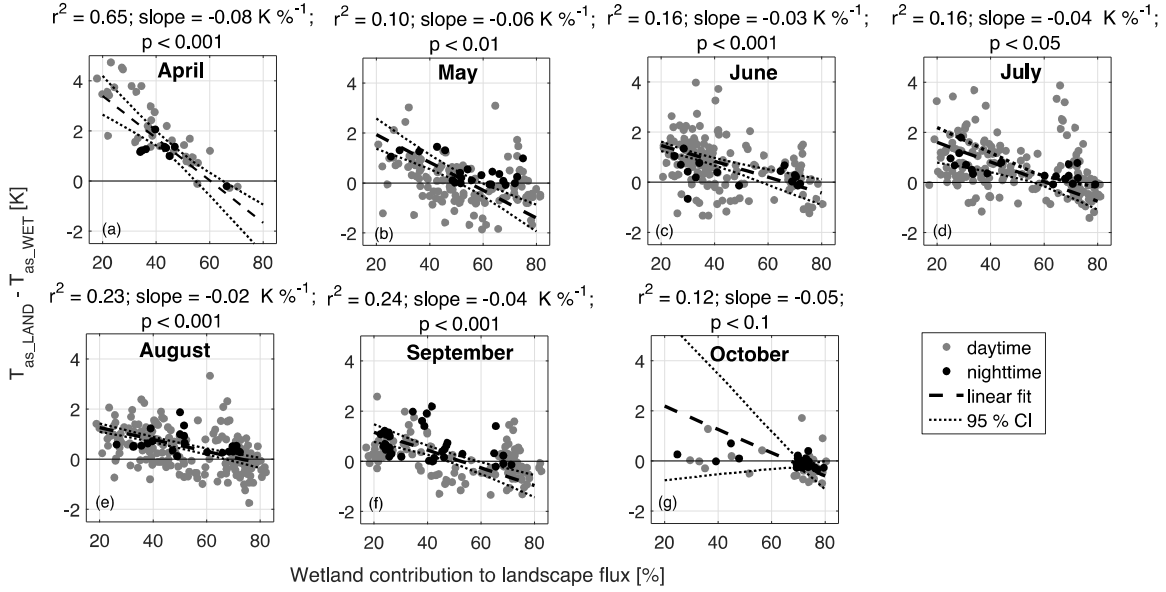

Fig. 4: Bulk aerodynamic conductance for heat in the footprints of the landscape and wetland tower. Colors of dots indicate contributions of wetlands to landscape tower fluxes. The total least square regression fit is shown as a solid black line. Dotted black lines indicate the 95 % confidence interval of the regression as derived from 1000 bootstrap simulations of the data.

Aerodynamic surface temperature

A surface cooling effect of wetlands between April and October 2014 is indicated by increasingly warmer T_{as} of the landscape tower footprints (T_{as_LAND}) compared to T_{as} of the wetland tower footprints (T_{as_WET}) with decreasing wetland contributions to the landscape footprints. The strongest cooling effect of 0.08 K per percent wetland contribution (K %$^{-1}$) was observed for the snow-cover period in April (Fig. 5a). During the snow-free period, wetland cooling ranged from 0.02 K %$^{-1}$ to 0.06 K %$^{-1}$ and coefficients of determination between differences in T_{as_LAND} and T_{as_WET} and wetland contributions to landscape fluxes increased from 0.10 in May to 0.24 in September (Figs. 5b-g). Both, day- and nighttime T_{as_LAND}, were warmer than T_{as_WET} in April. Nighttime T_{as_LAND} during the snow-free period was consistently warmer than T_{as_WET}, whereas daytime T_{as_LAND} was at times colder than T_{as_WET} (Fig. 5).

Fig. 5: Differences between aerodynamic surface temperatures of the landscape (T_{as_LAND}) and the wetland tower flux footprints (T_{as_WET}) as a function of wetland contributions to the landscape tower fluxes between April and October 2014. Day- (grey dots) and nighttime (black dots) differences are shown separately. Nighttime is defined as periods with less than 50 W m^{-2} incoming shortwave radiation. Best-fit lines with errors in both variables (York *et al.*, 2004) are shown as dashed lines. Dotted lines indicate the 95 % confidence intervals of best-fit lines as derived from 1000 bootstrap simulations of the data.

Surface conductance

In May and June 2013 and 2014, maximum bulk surface conductance (g_{s_0}; G_{s_bound} at a *VPD* of 0 kPa, see A3) increased from 7.2 mm s^{-1} (Fig. 6a & Tab. 1) for the "low wetland class" to 34.5 mm s^{-1} for the "high wetland class". In late summer, a similar increase was observed, but g_{s_0} for the high wetland class was reduced to 18.0 mm s^{-1}. The sensitivity of G_{s_bound} to *VPD* ($G_{s\_bound} = g_{s\_0}\ e^{(-b_d\ VPD)}$; see A3) was most pronounced for the "high wetland class" for May and June with the slope parameter b_d being 0.57 kPa^{-1}, whereas the "medium wetland class" had the strongest sensitivity of G_{s_bound} to *VPD* between July and August with a b_d of 0.48 kPa^{-1}. The "low wetland class" showed the lowest sensitivity during both periods with a b_d of 0.25 and 0.28 kPa^{-1} for the May-June and July-August periods, respectively (Tab. 1 & Fig. 6).

The limit of G_{s_bound} at infinite *SW$_{in}$* (g_{s_max} in $G_{s\_bound} = g_{s\_max}\ [SW_{in}\ /\ (b_{infl} + SW_{in})]$; see A3) increased with increasing flux footprints contributions from wetlands peaking at 33.8 mm s^{-1} in July and August for the "high wetland class". The inflection point of the G_{s_bound} vs. *SW$_{in}$* relationship (b_{infl} [W m^{-2}], see A3) ranged between 45.8 W m^{-2} and 1337.2 W m^2 and was always highest for the "high wetland class". However, b_{infl} between classes were not significantly different, except for b_{infl} for the "high wetland class" for July-August, which was significantly higher (Tab. 1). In July and August,

14

g_{s_max} and b_{infl} were poorly constrained for the "high wetland class" with 95 % CI of 138.1 mm s^{-1} and 7531.4 W m^{-2}, respectively (Fig. 6).

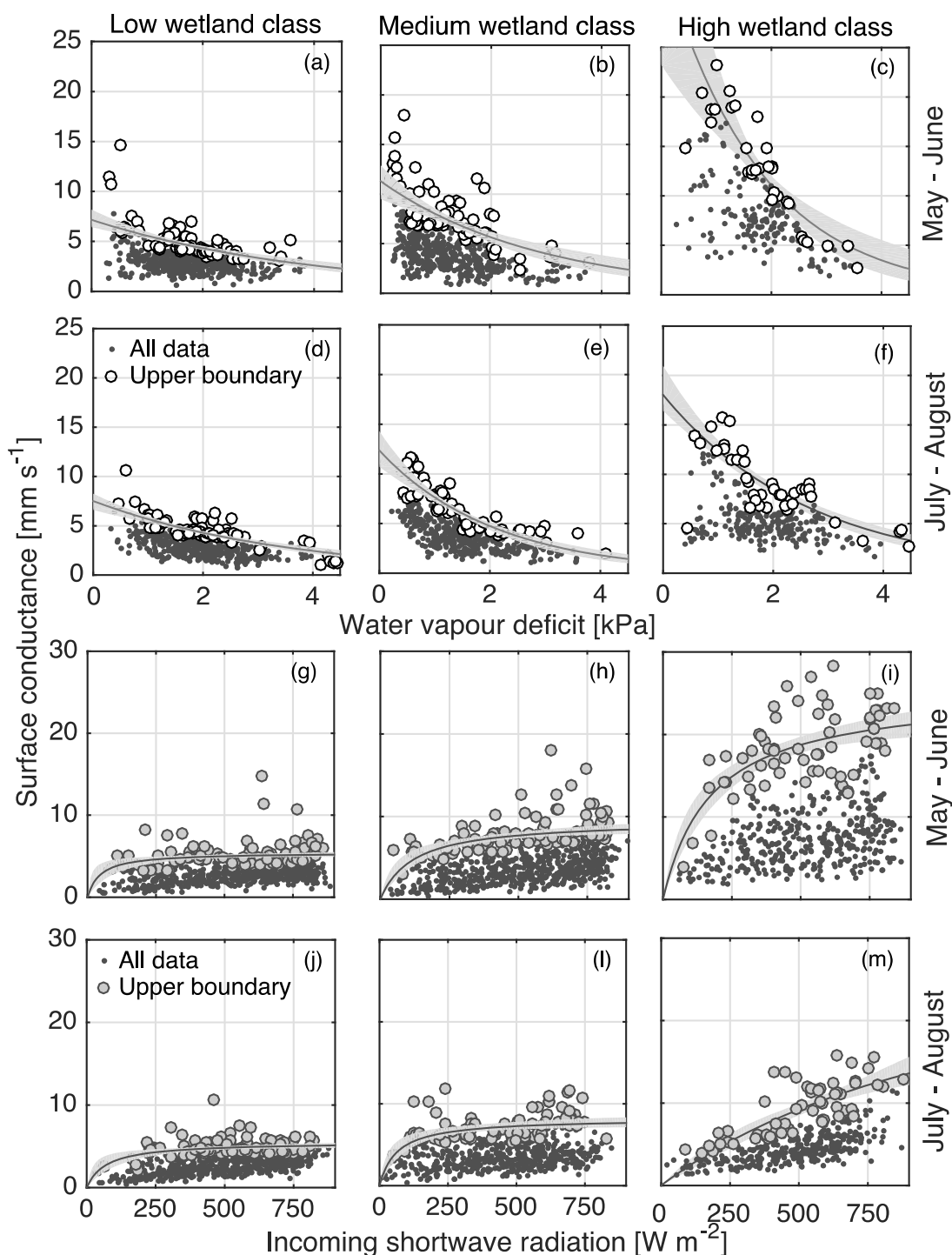**Tab. 1:** Best estimates and 95 % confidence intervals (CI) of a vapour pressure deficit ($G_{s\_bound} = g_{s0}\ e^{(-bd\ VPD)}$) ar
($G_{s\_bound} = g_{s\_max}\ [SW_{in}\ /\ (b_{infl} + SW_{in})]$) model of the upper boundary of bulk surface conductance (G_{s_bound})
August and for three classes of increasing permafrost-free wetland contribution to flux footprints. G_{s_bound} at
given by g_{s_0}, while b_d is a slope parameter. G_{s_bound} at infinite shortwave incoming radiation is given by $g_{s\_}$
(i.e. indicates the radiation value at which half of g_{s_max} is reached).

wetland class	vapour pressure deficit (VPD) model				incoming shortwave radiation (S\		
			May-June				
	g_{s_0} [mm s^{-1}]	95 % CI	b_d [kPa^{-1}]	95 % CI	g_{s_max} [mm s-1]	95 % CI	b_{infl} [W m-2]
low	7.2	6.4-8.2	0.25	0.19-0.32	5.5	5.1-6.1	45.8
medium	11.3	9.5-12.9	0.35	0.23-0.45	9.6	8.4-10.9	120.6
high	34.5	23.2-53.1	0.57	0.36-0.80	25.3	22.0-29.4	175.4
			July-August				
	g_{s_0} [mm s^{-1}]	95 % CI	b_d [kPa^{-1}]	95 % CI	$g_{\_s\_max}$ [mm s-1]	95 % CI	b_{infl} [W m-2]
low	7.5	6.6-8.3	0.28	0.22-0.33	5.5	4.9-6.2	71.4
medium	12.4	10.7-14.3	0.48	0.39-0.59	8.2	7.4-9.3	63.1
high	18.0	16.4-21.0	0.38	0.32-0.46	33.8	20.2-158.3	1337.2

Fig. 6: Response of bulk surface conductance to **(a-f)** vapour pressure deficit and **(g-m)** incoming shortwave radiation for the periods **(a-c & g-i)** May and June and **(d-f & j-m)** July and August for three classes of increasing permafrost-free wetland contributions ("low", "medium", "high"). Nonlinear model fits and 95 % confidence intervals of the models to the upper 15 % of bulk surface conductance per 0.5 kPa (white circles) and 100 W m^{-2} bins (gray circles) are shown as solid lines and shaded areas.
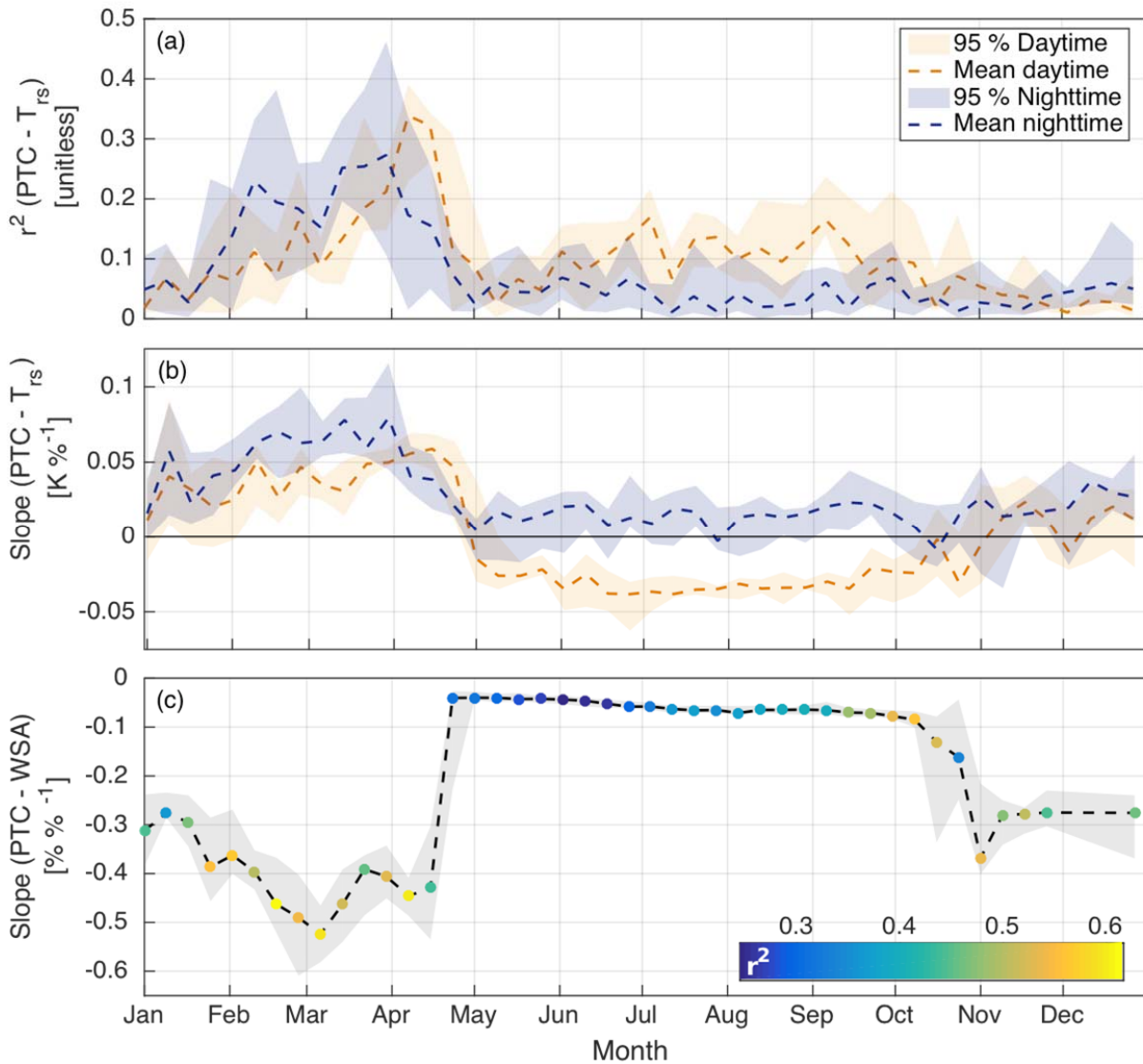
Regional-scale controls on surface properties in the lowlands of the southern Taiga Plains

To assess the regional-scale relationships between tree cover and day- and nighttime T_{rs} and albedo, we analysed 1-km MODIS percent tree cover, T_{rs}, and white-sky albedo between 2000 and 2015 for the southern Taiga Plains (Fig. 1b). The strongest relationships between day- and nighttime T_{rs} and tree cover were observed for March and April with r^2 of 0.34 and 0.27, respectively (Fig. 7a). Areas with high tree cover were characterised by warmer nighttime T_{rs} throughout the year with maximum nighttime T_{rs} sensitivities to tree cover of 0.08 K %$^{-1}$ at the end of March and consistently smaller sensitivities of ca. 0.01 K %$^{-1}$ between May and November (expressed as increase in K per one percent tree cover). Similarly, daytime T_{rs} increased with tree cover during the winter between November and April peaking at 0.06 K %$^{-1}$ in mid-April. In contrast, high tree cover areas were characterised by colder daytime T_{rs} between May and October compared to areas with low tree cover (negative slopes of up to -0.04 K %$^{-1}$, Fig. 7b).

The strongest relationships between day- and nighttime T_{rs} and tree cover in late winter coincided with the strongest relationship between tree cover and albedo (maximum slope of -0.55 % %$^{-1}$ in March; $r^2 = 0.62$; Fig. 7c). In April, slopes and r^2 between tree cover and albedo rapidly decreased and remained small until September before they gradually increased again to a slope of -0.38 % %$^{-1}$ and an r^2 of 0.36 in early November (Fig. 7c).

In comparison, tower-based T_{rs} for the forest and wetland between May and October 2014 indicate that median T_{rs} of the forest was 0.5 K colder and 1.7 K warmer than the wetland surface at 1030 MST and 2230 MST, respectively (Fig. S4). During late winter, just before snowmelt (13 - 30 April 2014), median T_{rs} of the forest was consistently warmer than T_{rs} of the wetland reaching 1.2 K and 1.8 K differences in T_{rs} at 1030 MST and 2230 MST, respectively (Fig. S4).

Fig. 7: **(a)** Seasonal dynamics of mean coefficients of determination (r^2) between 1-km percent tree cover (PTC; MODIS VCF MOD44B) and 1-km day- and nighttime radiometric surface temperature (T_{rs} at about 1230 & 0030 MST, respectively; MODIS Land Surface Temperature/Emissivity MOD11A2) for a ~4000 km^2 area in the southern Taiga Plains. **(b)** Seasonal dynamics of mean slopes of the regression between PTC and T_{s_rad}. **(c)** Seasonal dynamics of mean slopes between PTC and white-sky albedo (WSA, MODIS Albedo MOD43A3). Colors of dots represent mean r^2. Shaded areas indicate the 95 % confidence intervals of the means for the period 2000-2015. All slopes are significant at $\alpha = 0.001$.

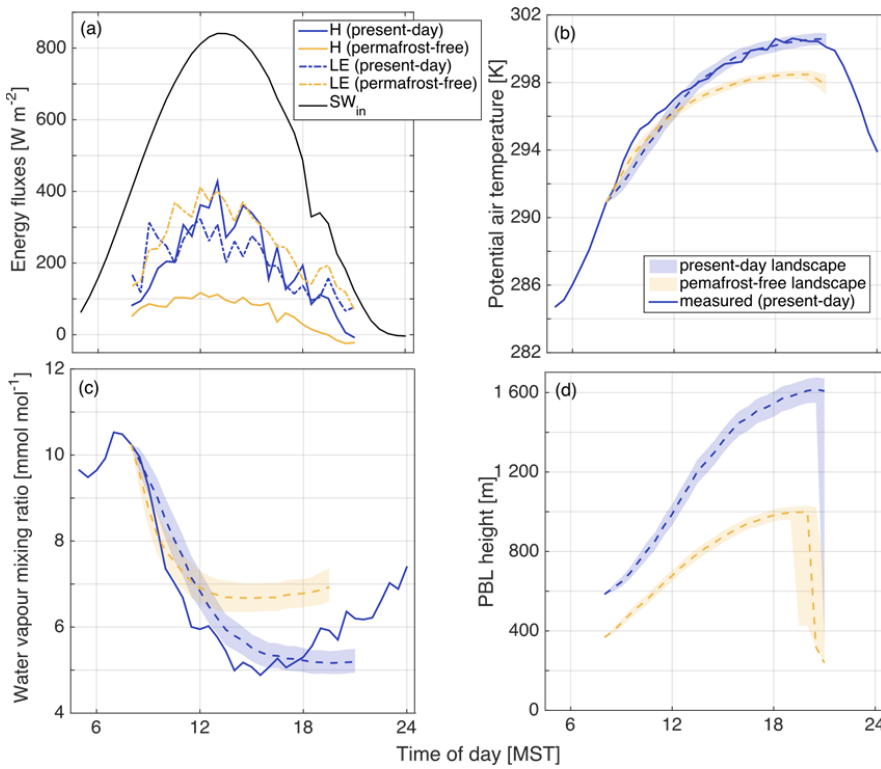**Permafrost thaw-induced boreal forest loss effects on regional air temperature and atmospheric moisture**

To estimate the potential effects of permafrost thaw-induced boreal forest loss on air temperature and atmospheric moisture, we modelled diurnal dynamics of PBL height, θ_m, and q_m for 49 clear-sky days in 2014 for two scenarios: a present-day heterogeneous boreal forest-wetland landscape ("present-day landscape") and a hypothetical homogeneous, permafrost-free, treeless wetland landscape ("permafrost-free landscape"). Results for one clear-sky day (22 June 2014) are discussed in detail.

Clear-sky conditions are usually characterised by a smooth diurnal curve of SW_{in} as observed on 22 June 2014 (Fig. 8a). The sensible heat flux for the present-day scenario peaked at 1300 MST. In comparison, the sensible heat flux for the permafrost-free scenario was consistently smaller and peaked at 1200 MST. For the permafrost-free scenario, LE was larger than LE for the present-day scenario between 1000 MST and 2030 MST and was slightly smaller during the morning hours (Fig. 8a).

Modelled θ_m fitted measured θ_m with a RMSE of 0.7 °C, while modelled q_m had a RMSE of 0.7 mmol mol^{-1}. For the present-day scenario, θ_m was 2.0 °C warmer and q_m 1.9 mmol mol^{-1} lower compared to the permafrost-free scenario at 2000 MST, just before the PBL collapsed (Fig. 8b & c).

The PBL height was consistently larger for the present-day scenario compared to the permafrost-free scenario with differences of up to around 600 m. The mean effective heat capacity of the PBL was 52 % higher for the present-day scenario than for the permafrost-free scenario. The entrainment of warm air from above the mixed layer accounted for 35 % and 54 % of the total sensible heat input to the mixed layer for the present-day and the permafrost-free scenario, respectively. Total sensible heat input from the entrainment layer just before the collapse of the PBL was 27 % larger for the permafrost-free scenario compared to the present-day scenario, mainly due to an enhanced gradient between θ_m and potential temperature of the entrainment layer in the permafrost-free scenario. The entrainment of dry air exceeded the input of water vapour from the surface for the present-day scenario causing a gradual decrease in q_m during the day. For the permafrost-free scenario, the entrainment of dry air exceeded the water vapour input from the surface until 1430 MST. Between 1500 MST and 2000 MST, q_m gradually increased since the surface water vapour input (LE) exceeded the entrainment of dry air.

Fig. 8: (a) Sensible (*H*) and latent (*LE*) heat fluxes for a present-day heterogeneous boreal forest-wetland landscape with sporadic permafrost ("present-day landscape") and for a permafrost-free wetland landscape scenario ("permafrost-free landscape") and incoming shortwave radiation (SW$_{in}$) for 22 June 2014. **(b)** Measured and modelled potential air temperatures in the mixed layer (θ_m). **(c)** Measured and modelled water vapour mixing ratios (q_m) and **(d)** modelled planetary boundary layer (PBL) heights. Shaded areas represent uncertainty due to random errors in flux measurements. q_m is modelled only for the time period before the PBL collapsed.

The largest mean differences in θ_m at 1800 MST between the present-day and the permafrost-free scenario were observed during April 2014 with θ_m being 3.6±2.4 °C (± one standard deviation; $n = 3$) colder for the permafrost-free scenario. During the summer, θ_m in the permafrost-free scenario was 1.25±0.8 °C and 1.58±0.9 °C colder for May & June ($n = 22$) and July & August ($n = 16$), respectively. In September, there was no significant difference between the permafrost-free and the present-day scenario with 0.02±1.4 °C ($n = 8$). Water vapour mixing ratios at 1800 MST were higher for the permafrost-free scenario throughout the observation period with maximum differences of 2.06±1.3 mmol mol^{-1} in July & August. Differences in q_m amounted to 1.42±1.2 mmol mol^{-1} in May & June and were small in April and September with 0.30±0.2 mmol mol^{-1} and 0.17±0.9 mmol mol^{-1}, respectively.

Discussion

Impacts of permafrost thaw on turbulent energy fluxes

Permafrost thaw-induced boreal forest loss in the sporadic permafrost zone is accelerating and is actively changing the vegetation composition and structure (e.g. Baltzer *et al.*, 2014; Helbig *et al.*, 2016; Lara *et al.*, 2016). However, little is known about the biophysical impacts of these changes on local- to regional-scale land-atmosphere interactions. Insights from global climate models are limited by their spatial resolution (Oleson *et al.*, 2004). Remote sensing approaches allow the assessment of biophysical impacts of deforestation on climate (e.g. surface and air temperature) across the globe (Li *et al.*, 2015; Alkama & Cescatti, 2016) and *in situ* measurements, such as from eddy covariance towers, in combination with local-scale modelling can be used to gain in-depth understanding of the underlying changes in ecosystem processes (Juang *et al.*, 2007; Vanden Broucke *et al.*, 2015; Stiegler *et al.*, 2016). Here, we combine landscape-scale eddy covariance measurements with regional-scale remote sensing data to quantify an atmospheric cooling and wetting effect of thaw-induced boreal forest loss.

Similar to the findings of our study, a decrease of about 50 % of annual H was observed for a fire-induced transition from a black spruce forest to bunch grasses in Alaska (Liu *et al.*, 2005) with the largest reduction at the end of the winter. In late winter, strongly increased albedo over treeless wetlands compared to forests leads to drastically reduced available energy following thaw-induced forest-to-wetland conversion. Liquid water is unavailable for LE until snowmelt, and all available energy is transferred to H (Betts *et al.*, 2001). During the summer, differences between boreal forest and wetland albedo are much smaller (e.g. Betts & Ball, 1997). Thus, larger H over the forested landscape compared to the wetland in the summer is mainly explained by drastically different partitioning of energy between coniferous forests and wetlands (Eugster *et al.*, 2000). Increased post-thaw LE and decreased Bowen ratios are consistent with an observed thaw-induced increase in soil moisture availability (Quinton *et al.*, 2011; Baltzer *et al.*, 2014). A similar change in the partitioning of available energy to LE following permafrost thaw was reported for a tundra ecosystem in northern Sweden (Stiegler *et al.*, 2016). In temperate and tropical regions, deforestation is generally leading to reductions in LE (Bala *et al.*, 2007). Similarly, Liu *et al.* (2005) reported a decrease in LE for the early post-fire treeless regeneration stages of a black spruce forest in Alaska. Thus, impacts of thaw-induced boreal forest loss on land-atmosphere interactions contrast deforestation impacts caused by fire disturbance or clear-cutting due to the associated shift toward higher post-thaw soil moisture.

In contrast to the strong direct control of wetland coverage on H_{LAND}, the direct control of wetland coverage on LE_{LAND} is less pronounced, indicating a more complex spatial pattern of water vapour fluxes across the landscape. Transpiration fluxes across the transition from wetlands to forests show a strong spatial heterogeneity (Baltzer *et al.*, 2014; Patankar *et al.*, 2015) and LE may also vary within wetlands due to spatial variations in water table position. Zoltai (1993) and Turetsky *et al.* (2007) showed that long-term peat accumulation leads to deeper water tables in the centre of collapse-scar bogs. At the recently thawed forest edges, the water table is closest to the moss surface enhancing the contribution of open water evaporation to LE. In contrast to the landscape tower, these transition

zones had only minor contributions to the wetland tower footprints. The complex spatial patterns in *LE* may reflect the small-scale heterogeneity of surface evaporation sources across boreal forest–wetland landscapes (Brown *et al.*, 2010; Angstmann *et al.*, 2013).

Permafrost thaw and landscape-scale changes in land surface properties

In a well-mixed PBL over heterogeneous landscapes with at disorganised surface structure at length scales <10 km such as Scotty Creek, atmospheric conditions (e.g. SW_{in}, VPD, T_{air}) over individual wetlands are similar to conditions over the larger boreal forest-wetland landscape (Shuttleworth, 1988; Garratt, 1994). Thus, contrasts in albedo, and eco-physiological and aerodynamic attributes between permafrost-free ecosystems (wetlands) and ecosystems with permafrost (forests) are the dominant drivers of the observed differences in turbulent energy fluxes.

In boreal forests, black spruce stands with low reflectance mask the highly reflective snow or ground cover (e.g. lichen, shrubs) resulting in a lower albedo compared to wetlands. The most pronounced albedo differences occur during the snow-cover period when the non-forested ecosystems (e.g. wetlands) are entirely covered by snow. The resulting higher available energy over forest stands (Betts & Ball, 1997; Liu *et al.*, 2005; Lohila *et al.*, 2010; Zhao & Jackson, 2014) indicates that albedo differences mainly induce the thaw-related decrease in *H* during this period. In the summer, with smaller albedo contrasts, differences in eco-physiological and aerodynamic properties enhance post-thaw *LE* and attenuate *H*.

Several studies have assessed the impacts of land-use and -cover changes on remotely sensed T_{rs} (e.g. Houspanossian *et al.*, 2013; Zhao & Jackson, 2014; Li *et al.*, 2015). However, T_{as} represents the surface temperature driving *H* and can substantially differ from T_{rs}, particularly in boreal forests with relatively sparse tree density, strong atmospheric coupling of the tree tops, and a ground surface that is more decoupled from the atmosphere (Sun & Mahrt, 1995; Friedl, 2002; Kustas *et al.*, 2006). We suggest that studies of forest loss impacts on remotely sensed T_{rs} should be complemented with analyses of T_{as} (e.g. derived from eddy covariance measurements) to better characterise the effects on local climate (e.g. Baldocchi & Ma, 2013). In this study, we show that thaw-induced forest loss leads to strong cooling of T_{as} and T_{rs} in late winter. In summer, a moderate cooling of T_{as} is observed, while remotely sensed T_{rs} indicates a daytime warming effect of forest loss for the same period. In contrast to tropical and temperate forests that are affected by large transpirational cooling (Bonan, 2008; Lee *et al.*, 2011), *LE* of black spruce forests is small (Baldocchi *et al.*, 2000). Thus, transpirational cooling of boreal forests is minimal (Lee *et al.*, 2011). At the same time, large *LE* over permafrost-free wetlands substantially cools the surface, which explains the lower T_{as} of the wetlands despite substantially lower g_H. Reductions in g_H and thus heat transfer efficiency with decreasing forest cover are consistent with lower aerodynamic roughness of low stature ecosystems, such as wetlands, compared to forests (Kelliher *et al.*, 1993; Juang *et al.*, 2007; Rotenberg & Yakir, 2010).

The thaw-induced decrease in Bowen ratios is mainly due to increased post-thaw soil moisture (Wright *et al.*, 2009; Baltzer *et al.*, 2014). In addition, the limited stomatal control of *LE* in wetlands dominated by *Sphagnum* and *Carex* species (Camill, 1999b) favours larger maximum g_s and consequently enhanced *LE*. Black spruce dominated boreal forests are characterised by consistently low g_s making them more drought resistant compared to other boreal tree species (Baldocchi *et al.*, 2000; Ewers *et al.*, 2005). Additionally, black spruce has a low light-saturation limit of photosynthesis, preventing stomata to open further at higher light levels (e.g. $SW_{in} > 400$ W m^{-2}; Kelliher *et al.*, 1993; Goulden *et al.*, 1997; Dang *et al.*, 1998; Baldocchi *et al.*, 2000). The drastic differences in soil moisture between forests and wetlands, the high *Sphagnum* coverage in wetlands, and their lack of stomatal control may explain the steady increase of g_s even at high light levels in wetlands (Nichols & Brown, 1980; Betts *et al.*, 1999; McFadden *et al.*, 2003). A similar permafrost thaw-induced reduction in soil moisture limitation on evapotranspiration and a simultaneous increase in g_s have been reported for a thawing tundra environment in Sweden by Stiegler *et al.* (2016).

Regional tree cover controls on surface characteristics

Decreasing tree cover in the southern Taiga Plains favours warmer daytime T_{rs} in summer contrasting the consistent cooling effect of thaw-induced forest loss on T_{as}. Such a warming effect of forest loss on daytime T_{rs} in summer was previously reported for the boreal zone (Li *et al.*, 2015). Similar to our study, Li *et al.* (2015) found a daytime T_{rs} cooling effect in winter and a year-round cooling effect on nighttime T_{rs}. Albedo is most sensitive to tree cover in late winter, when SW_{in} and Bowen ratios are high (Betts *et al.*, 2001; Liu *et al.*, 2005), indicating that albedo differences are the main cause for the observed cooling effect of forest and tree cover loss on T_{rs} (e.g. Betts, 2000; Zhao & Jackson, 2014; Li *et al.*, 2015). In contrast, the warming effect of forest and tree cover loss on daytime T_{rs} in the summer is likely caused by eco-physiological and aerodynamic effects exceeding the impacts of smaller summer albedo differences (e.g. Juang *et al.*, 2007). Transpirational cooling of forests is small and unlikely causing these patterns due to lower *LE* over forests compared to wetlands. To explain the warming effect of tree cover loss on daytime T_{rs} in the summer, we argue that, with increasing tree cover, ground surface shading is enhanced and sensible heat is more efficiently exchanged between the land surface and the atmosphere (e.g. Sun & Mahrt, 1995; Mahrt & Vickers, 2004). Remotely sensed T_{rs} is more strongly affected by the ground surface, which receives less SW_{in} beneath denser canopies due to below-canopy shading (Chasmer *et al.*, 2011a). The observed warming effect of tree cover loss on daytime T_{rs} suggests enhanced summertime soil heat input in areas characterised by declining tree cover. This warming effect is consistent with the absence of permafrost in mostly treeless wetlands and the occurrence of permafrost in forested plateaus (Zoltai, 1993; Quinton *et al.*, 2009).

Warmer nighttime T_{rs} in densely forested areas may be related to the nighttime biomass release of heat storage accumulated during the day (Lindroth *et al.*, 2010). Chasmer *et al.* (2011a) observed larger radiative cooling of open- compared to closed-canopy sites at Scotty Creek. Additionally, Lee *et al.* (2011) argue that forests are warmer at night because trees reduce the formation of stable stratification

allowing a more efficient transport of warm air from above to the surface. Our results highlight the importance to distinguish between T_{rs} and T_{as} when analysing land cover change impacts and to account for potentially contrasting effects between the snow and snow-free periods as well as between day- and nighttime observations.

Effects of permafrost thaw-induced boreal forest loss on air temperatures and atmospheric moisture

Due to the complex interactions of various biophysical impacts on near-surface climates (Betts *et al.*, 2001), previous studies demonstrated that forest loss appears to have either a cooling or a warming effect on surface air temperature (Juang *et al.*, 2007; Lee *et al.*, 2011; Mildrexler *et al.*, 2011; Alkama & Cescatti, 2016). Lee *et al.* (2011) observed warmer day- and nighttime air temperatures over mid- to high-latitude forests compared to nearby open land due to the combined effects of decreased albedo and increased surface roughness and Bowen ratios. Juang *et al.* (2007) showed that increased g_H of forests compared to agricultural fields can lead to a cooling effect of afforestation on surface temperature despite concurrent decreases in albedo. On a global scale, a warming effect of forest loss on air temperatures was explained by the decrease in surface roughness and reduced transpirational cooling with the conversion of forest to open land (e.g., Mildrexler *et al.*, 2011; Alkama & Cescatti, 2016). In this study, we show that thaw-induced boreal forest loss leads to a reduction of *H* and to an increase in *LE* (i.e. reducing Bowen ratios), exerting a cooling effect on regional air temperature along with an increase in atmospheric moisture.

Reduced diurnal *H* inputs to the PBL over permafrost-free wetlands are associated with a decrease in PBL depths compared to the typically deeper PBL depths characteristic for intact boreal forests (Betts *et al.*, 2001). More shallow PBL depths reduce the effective heat capacity of the PBL (Snyder *et al.*, 2004), generally amplify surface temperature variability (Esau *et al.*, 2012; Davy & Esau, 2014), and, thus, can have profound impacts on regional climates (Esau & Zilitinkevich, 2010). The large diurnal entrainment of warm and dry air into the PBL over boreal forests decreases q_m causing a surface-PBL feedback by further increasing *VPD*, inducing further decreases in g_s, resulting in enhanced partitioning of available energy to *H*, and eventually further PBL growth (Baldocchi *et al.*, 2000; Hill *et al.*, 2008). However, boreal forest loss and conversion to wetlands with high *Sphagnum* coverage decreases stomata control of *LE* and could slow down this positive feedback mechanism.

Changes in PBL depth, air temperature, and water vapour dynamics may also affect cloud formation and regional precipitation patterns (e.g. Juang *et al.*, 2007b). A decrease in air temperature and a concurrent increase in atmospheric moisture would result in a decrease of the lifting condensation level (height at which condensation of a lifting air parcel occurs) and could potentially increase cloud cover and the frequency of convective rainfall events (e.g. Betts, 2009). However, since thaw-induced boreal forest loss also leads to decreases in PBL depth, the probability of more frequent convective rainfall events may not increase if the PBL height stays below the lifting condensation level (Juang *et*

al., 2007b). Further research using more complex PBL models is required to better characterise the impacts of thaw-induced boreal forest loss on regional precipitation dynamics (e.g. Juang *et al.*, 2007b; de Arellano *et al.*, 2012).

Permafrost thaw and ultimately its disappearance are likely to continue to cause boreal forest loss and wetland expansion in the lowlands of the sporadic permafrost zone in North America. Similar to the southern Taiga Plains, accelerated thaw-induced forest loss has been reported for the Tanana Flats in central Alaska. However, there, loss was mainly attributed to decrease in birch forest coverage with a concurrent increase in wetland area (Lara *et al.*, 2016). The biophysical impacts of deciduous forest loss are likely to differ from the loss of coniferous forests (Juang *et al.*, 2007a), even when resulting in similar post-thaw wetland ecosystems. Deciduous forests are generally characterised by a higher albedo, a larger g_s, and larger LE compared to boreal coniferous forests (Betts & Ball, 1997; Baldocchi *et al.*, 2000; Liu *et al.*, 2005; Amiro *et al.*, 2006). Thus, to better understand how permafrost thaw-induced land cover change affects land-atmosphere interactions and consequently regional and global climates, the biophysical impacts of varying modes and pathways of permafrost thaw need to be assessed in addition to its biogeochemical impacts.

Acknowledgements

References

Alkama R, Cescatti A (2016) Biophysical climate impacts of recent changes in global forest cover. *Science*, **351**, 600–604.

Amiro B, Barr A, Black T et al. (2006) Carbon, energy and water fluxes at mature and disturbed forest sites, Saskatchewan, Canada. *Agricultural and Forest Meteorology*, **136**, 237–251.

Angstmann JL, Ewers BE, Barber J, Kwon H (2013) Testing transpiration controls by quantifying spatial variability along a boreal black spruce forest drainage gradient. *Ecohydrology*, **6**, 783–793.

de Arellano JV-G, van Heerwaarden CC, Lelieveld J (2012) Modelled suppression of boundary-layer clouds by plants in a CO_2-rich atmosphere. *Nature Geoscience*, **5**, 701–704.

Aylsworth JM, Kettles IM, Todd BJ (1993) Peatland distribution in the Fort Simpson area, Northwest Territories with a geophysical study of peatland-permafrost relationship at Antoine Lake. In: *Current Research, Part E*, pp. 141–148. Geological Survey of Canada.

Bala G, Caldeira K, Wickett M, Phillips TJ, Lobell DB, Delire C, Mirin A (2007) Combined climate and carbon-cycle effects of large-scale deforestation. *Proceedings of the National Academy of Sciences of the United States of America*, **104**, 6550–6555.

Baldocchi DD (2014) Measuring fluxes of trace gases and energy between ecosystems and the atmosphere - the state and future of the eddy covariance method. *Global Change Biology*, **20**, 3600-3609.

Baldocchi DD, Ma S (2013) How will land use affect air temperature in the surface boundary layer? Lessons learned from a comparative study on the energy balance of an oak savanna and annual grassland in California, USA. *Tellus B*, **65**, 19994.

Baldocchi DD, Kelliher FM, Black TA, Jarvis P (2000) Climate and vegetation controls on boreal zone energy exchange. *Global Change Biology*, **6**, 69–83.

Baltzer JL, Veness T, Chasmer LE, Sniderhan AE, Quinton WL (2014) Forests on thawing permafrost: fragmentation, edge effects, and net forest loss. *Global Change Biology*, **20**, 824–834.

Barr AG, Morgenstern K, Black TA, McCaughey JH, Nesic Z (2006) Surface energy balance closure by the eddy-covariance method above three boreal forest stands and implications for the

measurement of the CO_2 flux. *Agricultural and Forest Meteorology*, **140**, 322–337.

Betts RA (2000) Offset of the potential carbon sink from boreal forestation by decreases in surface albedo. *Nature*, **408**, 187–190.

Betts AK (2009) Land-surface-atmosphere coupling in observations and models. *Journal of Advances in Modeling Earth Systems*, **1**, 1–18.

Betts AK, Ball JH (1997) Albedo over the boreal forest. *Journal of Geophysical Research*, **102**, 28901–28909.

Betts AK, Goulden ML, Wofsy SC (1999) Controls on evaporation in a boreal spruce forest. *Journal of Climate*, **12**, 1601–1618.

Betts AK, Ball JH, McCaughey JH (2001) Near-surface climate in the boreal forest. *Journal of Geophysical Research*, **106**, 33529–33541.

Blanken PD, Black TA, Yang PC et al. (1997) Energy balance and canopy conductance of a boreal aspen forest: Partitioning overstory and understory components. *Journal of Geophysical Research*, **102**, 28915–289267.

Bonan GB (2008) Forests and climate change: forcings, feedbacks, and the climate benefits of forests. *Science*, **320**, 1444–1449.

Bonan GB, Pollard D, Thompson SL (1992) Effects of boreal forest vegetation on global climate. *Nature*, **359**, 716–718.

Brown SM, Petrone RM, Mendoza C, Devito KJ (2010) Surface vegetation controls on evapotranspiration from a sub-humid Western Boreal Plain wetland. *Hydrological Processes*, **24**, 1072–1085.

Camill P (1999a) Peat accumulation and succession following permafrost thaw in the boreal peatlands of Manitoba, Canada. *Écoscience*, **6**, 592–602.

Camill P (1999b) Patterns of boreal permafrost peatland vegetation across environmental gradients sensitive to climate warming. *Canadian Journal of Botany*, **77**, 721–733.

Camill P, Clark JS (1998) Climate change disequilibrium of boreal permafrost peatlands caused by local processes. *The American Naturalist*, **151**, 207–22.

Chapin FS, McGuire AD, Randerson J et al. (2000) Arctic and boreal ecosystems of western North America as components of the climate system. *Global Change Biology*, **6**, 211–223.

Chapin FS, Sturm M, Serreze MC et al. (2005) Role of land-surface changes in arctic summer warming. *Science*, **310**, 657–660.

Chasmer L, Quinton W, Hopkinson C, Petrone R, Whittington P (2011a) Vegetation canopy and radiation controls on permafrost plateau evolution within the discontinuous permafrost zone, Northwest Territories, Canada. *Permafrost and Periglacial Processes*, **22**, 199–213.

Chasmer L, Kljun N, Hopkinson C et al. (2011b) Characterizing vegetation structural and topographic characteristics sampled by eddy covariance within two mature aspen stands using lidar and a flux footprint model: Scaling to MODIS. *Journal of Geophysical Research: Biogeosciences*, **116**, G02026.

Chasmer L, Hopkinson C, Veness T, Quinton W, Baltzer J (2014) A decision-tree classification for low-lying complex land cover types within the zone of discontinuous permafrost. *Remote Sensing of Environment*, **143**, 73–84.

Connon RF, Quinton WL, Craig JR, Hayashi M (2014) Changing hydrologic connectivity due to permafrost thaw in the lower Liard River valley, NWT, Canada. *Hydrological Processes*, **28**, 4163–4178.

Dang Q-L, Margolis HA, Collatz GJ (1998) Parameterization and testing of a coupled photosynthesis-stomatal conductance model for boreal trees. *Tree Physiology*, **18**, 141–153.

Davin EL, de Noblet-Ducoudré N (2010) Climatic impact of global-acale deforestation: Radiative versus nonradiative processes. *Journal of Climate*, **23**, 97–112.

Davy R, Esau I (2014) Global climate models' bias in surface temperature trends and variability. *Environmental Research Letters*, **9**, 1–8.

Detto M, Montaldo N, Albertson JD, Mancini M, Katul G (2006) Soil moisture and vegetation controls on evapotranspiration in a heterogeneous Mediterranean ecosystem on Sardinia, Italy. *Water Resources Research*, **42**, W08419.

Dijk A Van, Moene AF, de Bruin HAR (2004) *The principles of surface flux physics: theory, practice and description of the ECPACK library, Internal Report 2004/1*. Wageningen, Netherlands, 99 pp.

Environment Canada (2014) Canadian Climate Normals: 1981 - 2010. URL http://climate.weather.gc.ca/climate_normals/index_e.html (accessed 23.11.2015).

Esau I, Davy R, Outten S (2012) Complementary explanation of temperature response in the lower atmosphere. *Environmental Research Letters*, **7**, 044026.

Esau I, Zilitinkevich S (2010) On the role of the planetary boundary layer depth in the climate system. *Advances in Science and Research*, **4**, 63–69.

Eugster W, Rouse WR, Pielke Sr RA et al. (2000) Land-atmosphere energy exchange in Arctic tundra and boreal forest: available data and feedbacks to climate. *Global Change Biology*, **6**, 84–115.

van Everdingen R (2005) *Multi-language glossary of permafrost and related ground-ice terms*. National Snow and Ice Data Center, Boulder, CO, 1-90 pp.

Ewers BE, Gower ST, Bond-Lamberty B, Wang CK (2005) Effects of stand age and tree species on canopy transpiration and average stomatal conductance of boreal forests. *Plant, Cell and Environment*, **28**, 660–678.

Fisher JB, Huntzinger DN, Schwalm CR, Sitch S (2014) Modeling the terrestrial biosphere. *Annual Review of Environment and Resources*, **39**, 91–123.

Friedl MA (2002) Forward and inverse modeling of land surface energy balance using surface temperature measurements. *Remote Sensing of Environment*, **79**, 344–354.

Foken T (2008) The energy balance closure problem: An overview. *Ecological Applications*, **18**, 1351–1367.

Garon-Labrecque M-E, Léveillé-Bourret É, Higgins K, Sonnentag O (2015) Additions to the boreal flora of the Northwest Territories with a preliminary vascular flora of Scotty Creek. *Canadian Field-Naturalist*, **129**, 349–367.

Garratt J (1994) Review: the atmospheric boundary layer. *Earth-Science Reviews*, **37**, 89–134.

Goulden ML, Daube BC, Fan S-M, Sutton DJ, Bazzaz A, Munger JW, Wofsy SC (1997) Physiological responses of a black spruce forest to weather. *Journal of Geophysical Research*, **102**, 28,987–28,996.

Grelle A, Lindroth A, Mölder M (1999) Seasonal variation of boreal forest surface conductance and

evaporation. *Agricultural and Forest Meteorology*, **98-99**, 563–578.

Gruber S (2012) Derivation and analysis of a high-resolution estimate of global permafrost zonation. *The Cryosphere*, **6**, 221–233.

Hartmann DL, Klein Tank AMG, Rusticucci M et al. (2013) Observations: Atmosphere and Surface. In: *Climate Change 2013: The Physical Science Basis. Contribution of Working Group I to the Fifth Assessment Report of the Intergovernmental Panel on Climate Change* (eds Stocker TF, Qin D, Plattner G-K, Tignor M, Allen SK, Boschung J, Nauels A, Xia Y, Bex V, Midgley PM), pp. 159–254. Cambridge University Press, Cambridge, United Kingdom and New York, NY, USA.

Hayashi M, Goeller N, Quinton WL, Wright N (2007) A simple heat-conduction method for simulating the frost-table depth in hydrological models. *Hydrological Processes*, **21**, 2610–2622.

Helbig M, Pappas C, Sonnentag O (2016) Permafrost thaw and wildfire: equally important drivers of boreal tree cover changes across the Taiga Plains, Canada. *Geophysical Research Letters*, **43**, 1598–1606.

Hill TC, Williams M, Moncrieff JB (2008) Modeling feedbacks between a boreal forest and the planetary boundary layer. *Journal of Geophysical Research*, **113**, D15122.

Houspanossian J, Nosetto M, Jobbágy EG (2013) Radiation budget changes with dry forest clearing in temperate Argentina. *Global Change Biology*, **19**, 1211–1222.

Igarashi Y, Kumagai T, Yoshifuji N et al. (2015) Environmental control of canopy stomatal conductance in a tropical deciduous forest in northern Thailand. *Agricultural and Forest Meteorology*, **202**, 1–10.

Jin Y, Randerson JT, Goetz SJ, Beck PSA, Loranty MM, Goulden ML (2012) The influence of burn severity on postfire vegetation recovery and albedo change during early succession in North American boreal forests. *Journal of Geophysical Research: Biogeosciences*, **117**, G01036.

Jorgenson MT, Racine CH, Walters JC, Osterkamp TE (2001) Permafrost degradation and ecological changes associated with a warming climate in central alaska. *Climatic Change*, **48**, 551–579.

Juang JY, Katul GG, Porporato A et al. (2007a) Eco-hydrological controls on summertime convective rainfall triggers. *Global Change Biology*, **13**, 887–896.

Juang JY, Katul G, Siqueira M, Stoy P, Novick K (2007b) Separating the effects of albedo from eco-physiological changes on surface temperature along a successional chronosequence in the southeastern United States. *Geophysical Research Letters*, **34**, L21408.

Kasurinen V, Alfredsen K, Kolari P et al. (2014) Latent heat exchange in the boreal and arctic biomes. *Global Change Biology*, **20**, 3439–3456.

Kelliher FM, Leuning R, Schulze ED (1993) Evaporation and canopy characteristics of coniferous forests and grasslands. *Oecologia*, **95**, 153–163.

Kljun N, Rotach MW, Schmid HP (2002) A three-dimensional backward Lagrangian footprint model for a wide range of boundary-layer stratifications. *Boundary-Layer Meteorology*, **103**, 205–226.

Kljun N, Calanca P, Rotach MW, Schmid HP (2004) A simple parameterisation for Flux Footprint Predictions. *Boundary-Layer Meteorology*, **112**, 503–523.

Kljun N, Calanca P, Rotach MW, Schmid HP (2015) A simple two-dimensional parameterisation for Flux Footprint Predictions (FFP). *Geoscientific Model Development*, **8**, 3695–3713.

Kustas WP, Anderson MC, Norman JM, Li F (2006) Utility of radiometric-aerodynamic temperature relations for heat flux estimation. *Boundary-Layer Meteorology*, **122**, 167–187.

Lara MJ, Genet H, McGuire AD et al. (2016) Thermokarst rates intensify due to climate change and forest fragmentation in an Alaskan boreal forest lowland. *Global Change Biology*, **22**, 816–829.

Lasslop G, Reichstein M, Kattge J, Papale D (2008) Influences of observation errors in eddy flux data on inverse model parameter estimation. *Biogeosciences*, **5**, 1311–1324.

Lee X, Goulden ML, Hollinger DY et al. (2011) Observed increase in local cooling effect of deforestation at higher latitudes. *Nature*, **479**, 384–387.

Li Y, Zhao M, Motesharrei S, Mu Q, Kalnay E, Li S (2015) Local cooling and warming effects of forests based on satellite observations. *Nature Communications*, **6**, 6603.

Lindroth A, Mölder M, Lagergren F (2010) Heat storage in forest biomass improves energy balance closure. *Biogeosciences*, **7**, 301–313.

Liu H, Randerson JT, Lindfors J, Chapin FS (2005) Changes in the surface energy budget after fire in boreal ecosystems of interior Alaska: An annual perspective. *Journal of Geophysical Research: Atmospheres*, **110**, D13101.

Lohila A, Minkkinen K, Laine J et al. (2010) Forestation of boreal peatlands: Impacts of changing albedo and greenhouse gas fluxes on radiative forcing. *Journal of Geophysical Research*, **115**, G04011.

Luyssaert S, Jammet M, Stoy PC et al. (2014) Land management and land-cover change have impacts of similar magnitude on surface temperature. *Nature Climate Change*, **4**, 389–393.

Mahrt L (2000) Surface heterogeneity and vertical structure of the boundary layer. *Boundary-Layer Meteorology*, **96**, 33–62.

Mahrt L, Vickers D (2004) Bulk formulation of the surface heat flux. *Boundary-Layer Meteorology*, **110**, 357–379.

Mauder M, Foken T (2011) *Documentation and Instruction Manual of the Eddy-Covariance Software Package TK3*. Bayreuth, Germany, 1-60 pp.

McFadden JP, Eugster W, Chapin FS (2003) A regional study of the controls on water vapor and CO_2 exchange in arctic tundra. *Ecology*, **84**, 2762–2776.

McNaughton KG, Spriggs TW (1986) A mixed-layer model for regional evaporation. *Boundary-Layer Meteorology*, **34**, 243–262.

Meissner KJ, Weaver AJ, Matthews HD, Cox PM (2003) The role of land surface dynamics in glacial inception: A study with the UVic Earth System Model. *Climate Dynamics*, **21**, 515–537.

Mildrexler DJ, Zhao M, Running SW (2011) A global comparison between station air temperatures and MODIS land surface temperatures reveals the cooling role of forests. *Journal of Geophysical Research*, **116**, G03025.

Moncrieff JB, Massheder JM, de Bruin H et al. (1997) A system to measure surface fluxes of momentum, sensible heat, water vapour and carbon dioxide. *Journal of Hydrology*, **188-189**, 589–611.

Moncrieff JB, Malhi Y, Leuning R (1996) The propagation of errors in long-term measurements of land-atmosphere fluxes of carbon and water. *Global Change Biology*, **2**, 231–240.

Moncrieff J, Clement R, Finnigan J, Meyers T (2004) Averaging, detrending, and filtering of eddy covariance time series. In: *Handbook of Micrometeorology* (eds Lee X, Massman WJ, Law B), pp. 7–31. Springer Netherlands, Amsterdam, The Netherlands.

Nakai T, Kim Y, Busey RC et al. (2013) Characteristics of evapotranspiration from a permafrost black spruce forest in interior Alaska. *Polar Science*, **7**, 136–148.

National Wetlands Working Group (1997) *The Canadian Wetland Classification System*, 2nd edn (eds Warner BG, Rubec CDA). University of Waterloo, Waterloo, Ontario, 68 pp.

Nichols DS, Brown JM (1980) Evaporation from a Sphagnum moss surface. *Journal of Hydrology*, **48**, 289–302.

Oleson KW, Bonan GB, Levis S, Vertenstein M (2004) Effects of land use change on North American climate: Impact of surface datasets and model biogeophysics. *Climate Dynamics*, **23**, 117–132.

Olson DM, Dinerstein E, Wikramanayake ED et al. (2001) Terrestrial ecoregions of the world: A new map of life on earth. *BioScience*, **51**, 933–938.

Papale D, Reichstein M, Aubinet M et al. (2006) Towards a standardized processing of Net Ecosystem Exchange measured with eddy covariance technique: algorithms and uncertainty estimation. *Biogeosciences*, **3**, 571–583.

Patankar R, Quinton WL, Hayashi M, Baltzer JL (2015) Sap flow responses to seasonal thaw and permafrost degradation in a subarctic boreal peatland. *Trees*, **29**, 129–142.

Quinton WL, Baltzer JL (2013) The active-layer hydrology of a peat plateau with thawing permafrost (Scotty Creek, Canada). *Hydrogeology Journal*, **21**, 201–220.

Quinton WL, Hayashi M, Chasmer LE (2009) Peatland hydrology of discontinuous permafrost in the Northwest Territories: Overview and Synthesis. *Canadian Water Resources Journal*, **34**, 311–328.

Quinton WL, Hayashi M, Chasmer LE (2011) Permafrost-thaw-induced land-cover change in the Canadian subarctic: implications for water resources. *Hydrological Processes*, **25**, 152–158.

Randerson JT, Liu H, Flanner MG et al. (2006) The impact of boreal forest fire on climate warming. *Science*, **314**, 1130–1132.

Reichstein M, Falge E, Baldocchi D et al. (2005) On the separation of net ecosystem exchange into assimilation and ecosystem respiration: review and improved algorithm. *Global Change Biology*, **11**, 1424–1439.

Rossby CG, Montgomery RB (1935) The layer of frictional influence in wind and ocean currents. *Papers in Physical Oceanography and Meteorology*, **3**, 1–101.

Rotenberg E, Yakir D (2010) Contribution of semi-arid forests to the climate system. *Science*, **327**, 451–454.

Schaepman-Strub G, Schaepman ME, Painter TH, Dangel S, Martonchik J V. (2006) Reflectance quantities in optical remote sensing-definitions and case studies. *Remote Sensing of Environment*, **103**, 27–42.

Schmid HP (1997) Experimental design for flux measurements: matching scales of observations and fluxes. *Agricultural and Forest Meteorology*, **87**, 179–200.

Shuttleworth WJ (1988) Macrohydrology - The new challenge for process hydrology. *Journal of Hydrology*, **100**, 31–56.

Snyder PK, Delire C, Foley JA (2004) Evaluating the influence of different vegetation biomes on the global climate. *Climate Dynamics*, **23**, 279–302.

Stiegler C, Johansson M, Christensen TR, Mastepanov M, Lindroth A (2016) Tundra permafrost thaw causes significant shifts in energy partitioning. *Tellus B*, **68**, 30467.

Stoy PC, Mauder M, Foken T et al. (2013) A data-driven analysis of energy balance closure across FLUXNET research sites: The role of landscape scale heterogeneity. *Agricultural and Forest Meteorology*, **171-172**, 137–152.

Strong WL, Zoltai SC, Ironside G. (1989) *Ecoclimatic regions of Canada*, Ecological edn, Vol. 23. Canadian Wildlife Service, Ottawa, 122 pp.

Sun J, Mahrt L (1995) Relationship of surface heat flux to microscale temperature variations: Application to BOREAS. *Boundary-Layer Meteorology*, **76**, 291–301.

Tarnocai C (2006) The effect of climate change on carbon in Canadian peatlands. *Global and Planetary Change*, **53**, 222–232.

Turetsky MR, Wieder RK, Vitt DH, Evans RJ, Scott KD (2007) The disappearance of relict permafrost in boreal north America: Effects on peatland carbon storage and fluxes. *Global Change Biology*, **13**, 1922–1934.

Twine TE, Kustas WP, Norman JM et al. (2000) Correcting eddy-covariance flux underestimates over a grassland. *Agricultural and Forest Meteorology*, **103**, 279–300.

Vanden Broucke S, Luyssaert S, Davin EL, Janssens I, van Lipzig N (2015) New insights in the capability of climate models to simulate the impact of LUC based on temperature decomposition of paired site observations. *Journal of Geophysical Research: Atmospheres*, **120**.

Vickers D, Mahrt L (1997) Quality Control and Flux Sampling Problems for Tower and Aircraft Data. *Journal of Atmospheric and Oceanic Technology*, **14**, 512–526.

Wan Z (2014) New refinements and validation of the MODIS Land-Surface Temperature/Emissivity products. *Remote Sensing of Environment*, **140**, 36–45.

Webb EK, Pearman GI, Leuning R (1980) Correction of flux measurements for density effects due to heat and water vapour transfer. *Quarterly Journal of the Royal Meteorological Society*, **106**, 85–100.

Wilczak JM, Oncley SP, Stage SA (2001) Sonic anemometer tilt correction algorithms. *Boundary-Layer Meteorology*, **99**, 127–150.

Wilson K, Goldstein A, Falge E et al. (2002) Energy balance closure at FLUXNET sites. *Agricultural and Forest Meteorology*, **113**, 223–243.

Wohlfahrt G, Haslwanter A, Hörtnagl L, Jasoni RL, Fenstermaker LF, Arnone J a., Hammerle A (2009) On the consequences of the energy imbalance for calculating surface conductance to water vapour. *Agricultural and Forest Meteorology*, **149**, 1556–1559.

Wright N, Hayashi M, Quinton WL (2009) Spatial and temporal variations in active layer thawing and their implication on runoff generation in peat-covered permafrost terrain. *Water Resources Research*, **45**, W05414.

York D, Evensen NM, López M, Delgado JDB (2004) Unified equations for the slope, intercept, and standard errors of the best straight line. *American Journal of Physics*, **72**, 367–375.

Zhao K, Jackson RB (2014) Biophysical forcings of land-use changes from potential forestry activities in North America. *Ecological Monographs*, **84**, 329–353.

Zoltai SC (1993) Cyclic Development of permafrost in the peatlands of Northwestern Canada. *Arctic and Alpine Research*, **25**, 240–246.

Zoltai SC, Tarnocai C (1975) Perennially frozen peatlands in the western Arctic and Subarctic of Canada. *Canadian Journal of Earth Sciences*, **12**, 28–43.

Cooling effect of thaw-induced forest loss

Appendix

A1 Footprint modelling

The 2-D flux footprint parameterisation of Kljun *et al.* (2015) was applied for the landscape tower for half-hours with roughness lengths smaller than 0.95 m. With larger roughness lengths, the eddy covariance instruments were within the roughness sublayer, where measurements at one fixed point are not representative due to horizontally varying flux magnitudes (Mahrt, 2000). The eddy covariance system at the wetland tower was always above the roughness sublayer. The relative flux contribution matrices were projected on a LiDAR/fusion-based land cover classification with discrete classes for forests, wetlands and thaw lakes, and a LiDAR-derived canopy height map, both derived from remote sensing (Chasmer *et al.*, 2014, Fig. 1c).

A2 Surface energy balance closure at the landscape and the wetland tower

Sums of *H* and *LE* as measured by the eddy covariance technique were shown to be consistently smaller than available energy (i.e. lack of land surface EBC) across different ecosystems and instrumental setups (e.g. Wilson *et al.*, 2002; Stoy *et al.*, 2013). The reported discrepancies could either be caused by an overestimation of the available energy or an underestimation of turbulent energy fluxes (e.g. Foken, 2008a). To ensure the comparability of *H* and *LE* at the landscaoe and the wetland tower, the EBC at the two sites was assessed as follows:
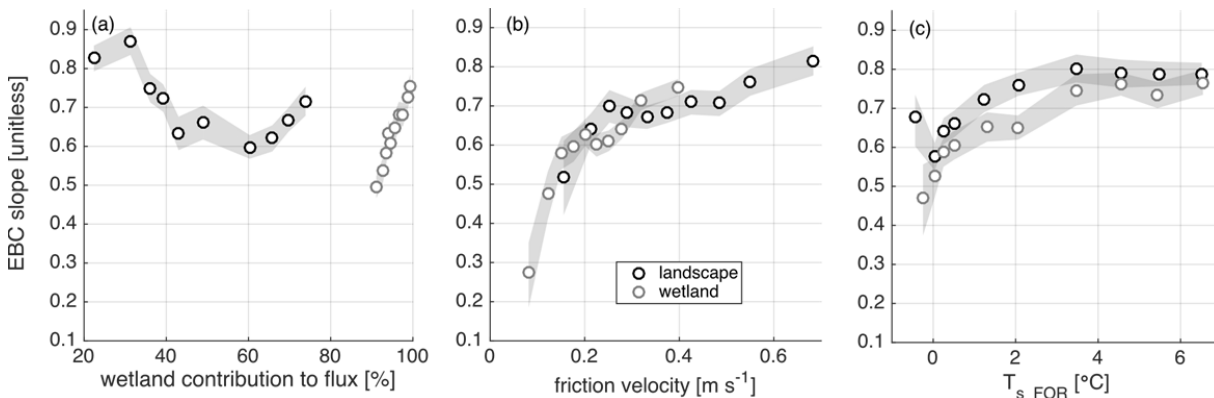
$$H + LE = R_n - G - S - Q_m - C \qquad (1)$$

where R_n is net radiation [W m^{-2}], G is the soil heat flux [W m^{-2}], S is the rate of change of heat storage in the air column below the measurement height [W m^{-2}], as derived from one-point changes in T_a and specific humidity [q_a; kg kg^{-1}], Q_m is the snow melt energy flux [W m^{-2}], and C [W m^{-2}] is the closure term for measurement errors or missing terms (e.g. soil thaw). Heat storage in biomass and the energy flux related to photosynthesis were assumed to be negligible due to the typically low productivity and low biomass of northern boreal forests (Baldocchi *et al.*, 2000; Wilson *et al.*, 2002). No storage term was calculated for the consumption or release of energy for thawing and freezing of the soil above the heat flux plates.

Since the flux footprints of the landscape tower mainly consisted of forests and wetlands, the available energy was calculated as a weighted average of the ecosystem-scale measurements of R_n, G, and Q_m at the wetland and the landscape tower. The weights were estimated for each half hour as the relative contribution of these two land cover types to the flux measurements, quantified with the 2-D

footprint parameterisation of Kljun *et al.* (2015) (see also Chasmer *et al.* (2011b) and Detto *et al.* (2006).

The EBC for the landscape and the wetland tower (defined as the slope of available energy against the sum of turbulent energy fluxes) scale with the contribution of wetlands to the flux measurements, with friction velocity (u_*; m s^{-1}), and soil temperatures at 20 cm in the forest (T_{s_FOR}; ºC) (Fig. A1). We assume that the relationship of the EBC with T_{s_FOR} is caused by an underestimation of *G* early in the season due to the omission of a soil thaw energy flux (e.g. Betts *et al.*, 1999; Nakai *et al.*, 2013). In contrast, the dependence of EBC on u_* is likely caused by underestimated *H* and *LE* (e.g. Barr *et al.*, 2006). For periods with T_{s_FOR} above 3 ºC, u_* above 0.2 m s^{-1}, and wetland tower footprint contributions from the wetland larger than 95 %, EBC was 0.79 and 0.78 for the landscape and the wetland tower, respectively. We therefore removed flux measurements from both towers when u_* was below 0.2 m s^{-1}, and for the wetland tower when the wetland contribution to the flux footprint was less than 95 % (i.e. footprints extended into surrounding forest). For the landscape tower, data coverage was 50 % for *H* and *LE* in 2013 (12 May 2013 – 01 November 2013). In 2014 (13 April 2014 – 07 November 2014), data coverage was 52 % for *H* and *LE* at the landscape tower and 20 % for *H* and *LE* at the wetland tower.

Fig. A1: Slope of the energy balance closure (EBC) for the landscape and the wetland tower as function of **(a)** permafrost-free wetland contributions to flux footprints, **(b)** friction velocity, and **(c)** soil temperature at 20 cm on the forested permafrost plateau (T_{s_FOR}). Shaded areas show the 95 % confidence interval of the slopes.

A3   Atmospheric controls of surface conductance

Non-linear VPD and SW_{in} models were fitted to g_s for half-hours with low wetland contributions to landscape tower footprints (FR_{WET}) (FR_{WET} < median of FR_{WET} [63 %]), to g_s with high FR_{WET} (FR_{WET} ≥ median of FR_{WET} [63 %]), and to g_s derived from fluxes at the wetland tower (contributions from wetlands ≥95 %). Only daytime g_s (0900 and 2100 MST) and g_s for periods with LE >10 W m^{-2} were used, since the expression of g_s becomes numerically unstable when LE <10 W m^{-2}. The VPD control on G_{s_bound} was modelled as follows (e.g. Blanken *et al.*, 1997):

$$G_{s\_bound\_i} = g_{s0\_i}\, e^{(-b_d\, VPD)} \qquad\qquad (A1)$$

where i stands for the i-th dataset class, g_{s0} (m s^{-1}) is the bulk surface conductance at a VPD of 0 kPA, and b_d indicates the sensitivity of G_{s_bound} to VPD (kPa^{-1}). The model was fitted to the upper 15 % of g_s per 0.5 kPa VPD window. Data for periods with SW_{in} <300 W m^{-2} were excluded to avoid radiation-controlled g_s.

The dependence of G_{s_bound} on SW_{in} was modelled using a Michaelis-Menten function (e.g. Grelle *et al.*, 1999):

$$G_{s\_max\_i} = g_{s\_\mathrm{max}\_i}\, \frac{SW_{in}}{b_{infl}+SW_{in}} \qquad\qquad (A2)$$

where g_{s_max} is the upper limit of g_s at high SW_{in} and b_{infl} is a parameter defining SW_{in} when G_{s_bound} reaches half of its upper limit. To assess the radiation-dependence of G_{s_bound}, only periods with VPD >0.3 kPa were analysed to ensure that g_s was not controlled by VPD. Uncertainties of the model fits were quantified by fitting the model to 1000 bootstrap realisations of the datasets.

A4   The planetary boundary layer model

The time rate of change in potential air temperature of the mixed layer ($\frac{d\theta_m}{dt}$; K s^{-1}) resulting from input of sensible heat from the surface (H) and from entrainment of warm air above the temperature inversion at the top of the mixed layer was modelled using Eqn. 1 in McNaughton & Spriggs (1986). The time rate of change in q_m was calculated using Eqn. 2 in McNaughton & Spriggs (1986). Eqn. 10 in McNaughton & Spriggs (1986) was used to model the time rate of change in PBL height:

$$\frac{dh}{dt} = \frac{H_v}{\rho C_p h \Gamma_v} \qquad\qquad (13)$$

The vertical gradient of virtual potential air temperature [lapse rate; K m^{-1}] was taken as the lapse rate of moist air of 0.0065 K m^{-1}.

To model θ_m at the landscape tower, we used H and LE from the landscape tower as forcing. Modelled θ_m and q_m can only be compared to measured θ_m and q_m when H and LE at the landscape tower are representative of the energy fluxes affecting instantaneous PBL dynamics, which is not

always the case over a heterogeneous landscape. Only days with clear-sky conditions and a total sum of less than five half-hours of missing or low quality (quality flag >1) H and LE at the landscape and the wetland tower were included in the analysis. Remaining gaps were filled using linear interpolation and days with an RMSE of the modelled θ_m >2 K were discarded to ensure good model performance. The analysis of the EBC indicated an average underestimation of ~20 % of the sum of H and LE (see above). Therefore, we corrected for this underestimation in our model by increasing the measured H and LE accordingly assuming that the lack of EBC was equally caused by H and LE (Twine *et al.*, 2000; Wohlfahrt *et al.*, 2009).

Air temperature and water vapour mixing ratio at Scotty Creek were only measured in the mixed layer and, thus, θ_e and q_e were not known. Potential air temperature and q_e above the entrainment layer was derived numerically by minimising the RMSE of modelled θ_m and q_m versus measured θ_m and q_m at the landscape tower. Friction velocity was used to calculate the initial PBL height (Rossby & Montgomery, 1935).